



2007

REFLECTED IMAGE PROCESSING FOR SPECULAR WELD POOL SURFACE MEASUREMENT

Aparna Janga

University of Kentucky, aparna.janga@uky.edu

[Right click to open a feedback form in a new tab to let us know how this document benefits you.](#)

Recommended Citation

Janga, Aparna, "REFLECTED IMAGE PROCESSING FOR SPECULAR WELD POOL SURFACE MEASUREMENT" (2007). *University of Kentucky Master's Theses*. 502.
https://uknowledge.uky.edu/gradschool_theses/502

This Thesis is brought to you for free and open access by the Graduate School at UKnowledge. It has been accepted for inclusion in University of Kentucky Master's Theses by an authorized administrator of UKnowledge. For more information, please contact UKnowledge@lsv.uky.edu.

ABSTRACT OF THESIS

REFLECTED IMAGE PROCESSING FOR SPECULAR WELD POOL SURFACE MEASUREMENT

The surface of the weld pool contains information that can be exploited to emulate a skilled human welder to better understand and control the welding process. Of the existing techniques, the method that uses the pool's specular nature to an advantage and which is relatively more cost effective, and suitable for welding environment is the one that utilizes reflected images to reconstruct 3D weld pool surface by using structured light and image processing techniques. In this thesis, an improvement has been made to the existing method by changing welding direction to obtain a denser reflected dot-matrix pattern allowing more accurate surface measurement. Then, the reflected images, obtained by capturing the reflection of a structured laser dot-matrix pattern from the pool surface through a high-speed camera with a narrow band-pass filter, are processed by a newly proposed algorithm to find the position of each reflected dot relative to its actual projection dot. This is a complicated process owing to the increased density of dots and noise induced due to the harsh environment. The obtained correspondence map may later be used by a surface reconstruction algorithm to derive the three-dimensional pool surface based on the reflection law.

KEYWORDS: GTAW, Specular surface, Reflected Images, Wavelet Transform, Position Analysis

Aparna Janga

12/12/07

REFLECTED IMAGE PROCESSING FOR SPECULAR WELD POOL SURFACE
MEASUREMENT

By

Aparna Janga

YuMing Zhang

Director of Thesis

YuMing Zhang

Director of Graduate Studies

12/12/07

Date

RULES FOR THE USE OF THESES

Unpublished theses submitted for the Master's degree and deposited in the University of Kentucky Library are as a rule open for inspection, but are to be used only with due regard to the rights of the authors. Bibliographical references may be noted, but quotations or summaries of parts may be published only with the permission of the author, and with the usual scholarly acknowledgments.

Extensive copying or publication of the thesis in whole or in part also requires the consent of the Dean of the Graduate School of the University of Kentucky.

A library that borrows this thesis for use by its patrons is expected to secure the signature of each user.

NameDate[illegible]

THESIS

Aparna Janga

The Graduate School

University of Kentucky

2007

REFLECTED IMAGE PROCESSING FOR SPECULAR WELD POOL SURFACE MEASUREMENT

THESIS

A Thesis submitted in partial fulfillment of the
requirements for the degree of Master of Science in the
College of Engineering
at the University of Kentucky

By

Aparna Janga

Lexington, Kentucky

Director: Dr. YuMing Zhang, Professor of Electrical Engineering

Lexington, Kentucky

2007

Copyright © Aparna Janga 2007

This thesis is dedicated to my family

ACKNOWLEDGEMENTS

With immense pleasure I take this opportunity to thank one and all who have helped me in making this project successful.

Firstly, I would like to sincerely thank Dr. YuMing Zhang for his valuable guidance, constant encouragement during the entire period of this thesis work.

Next, I thank Hongsheng Song for his help through thought provoking discussions, valuable suggestions and instructive comments at every stage of this thesis process.

Third, this research is funded by the National Science Foundation under grant CMMI-0527889.

Finally I am grateful to my family for their love and support throughout my life. I would also like to express my deep sense of gratitude to my friend Sriramphani Garimella for his unending love, support and encouragement. I also appreciate the valuable time he spent in giving technical assistance and comments that helped me complete this project well in time.

TABLE OF CONTENTS

Acknowledgements.....	iii
List of Tables.....	vi
List of Figures.....	vii
List of Files.....	xi
CHAPTER 1: INTRODUCTION.....	1
1.1 Overview of GTAW.....	1
1.2 X-ray Radiation.....	3
1.3 Ultrasonic Technique.....	3
1.4 Weld Pool Sensing Technique.....	4
1.5 Acoustic Emission Sensing Technique.....	4
1.6 Thermal Sensing Technique.....	5
1.7 Weld Pool Oscillation Sensing.....	5
1.8 Vision Based Sensing.....	6
1.8.1 Two-dimensional Observation and Analysis.....	6
1.8.2 Three-dimensional Observation and Analysis.....	8
1.9 Thesis Objective.....	12
1.10 Thesis Outline.....	13
CHAPTER 2: SYSTEM REVIEW.....	15
2.1 Diffuse Reflection.....	15
2.2 Specular Reflection.....	16
2.3 Experimental Setup.....	18
2.4 Algorithm and Results.....	24
CHAPTER 3: IMPROVEMENT OF THE SYSTEM.....	27
CHAPTER 4: FEATURE EXTRACTION.....	34
4.1 DC Level Shift.....	35
4.2 Noise Removal using Wavelet Transform.....	35
4.3 Image Segmentation.....	43
4.3.1 Edge Detection.....	44

4.3.2 Thresholding.....	46
CHAPTER 5: POSITION ANALYSIS OF REFLECTED DOTS.....	51
5.1 Flowchart of the Algorithm.....	51
5.2 Grouping of Dots According to Their Respective Rows.....	52
5.3 Extracting the Dots of Each Row.....	58
5.4 Identification and Deletion of Rows Blocked by the Torch.....	64
5.5 Detect the Row with One Missing Dot.....	65
5.6 Updating the column numbers.....	69
5.7 Results.....	75
CHAPTER 6: CONCLUSION AND FUTURE WORK.....	88
REFERENCES.....	90
VITA.....	95

LIST OF TABLES

Table 5-1 Matrix storing the row, column and position information of each dot...	59
Table 5-2 Matrix storing the highest positioned dot in each row.....	61
Table 5-3 Matrix with rows sorted according to the highest positioned dots.....	62
Table 5-4 Matrix with the updated row numbers.....	63
Table 5-5 Matrix storing the information of first and last dot of each row, average distance between dots, total number of dots and highest positioned dot.....	64
Table 5-6 Matrix with discontinuities in the rows fixed.....	66
Table 5-7 Matrix with correct row numbers and updated missing dot position...	68
Table 5-8 Finding the dots corresponding to the reference dot.....	72
Table 5-9 Final matrix with correct row and column numbers.....	74

LIST OF FIGURES

Figure 1-1 Different penetration statuses (profiles) in the welding process [6] [13].....	2
Figure 1-2 Ultrasonic penetration sensing system [15] [6].....	3
Figure 1-3 Experimental set up and the acquired image [7] [6].....	6
Figure 1-4 Weld pool geometry at current of 90 A and speed of 103mm/s [21] [6].....	8
Figure 1-5 Weld pool geometry at current of 100 A and speed of 113mm/s [21] [6].....	8
Figure 1-6 Experiment scheme and image acquired under high power pulsed Laser [8] [6].....	9
Figure 1-7 Simulation of 3D weld pool surface (a) Approximation of reflection point (b) Estimated weld pool surface from slope field [27] [6].....	11
Figure 1-8 A captured reflected dot-matrix image [6].....	11
Figure 1-9 Illustration of correspondence relationship between projected and reflected dots.....	12
Figure 2-1 Diffuse reflection [6].....	15
Figure 2-2 Specular reflection [6].....	16
Figure 2-3 Multiple-line pattern and its application in the system [6].....	17
Figure 2-4 Image of reflected Laser Line pattern on a mild steel work piece. [6].....	18
Figure 2-5 Experimental setup for obtaining reflected images of the specular surface of GTAW pool [6].....	19
Figure 2-6 Welded Work piece [6].....	20
Figure 2-7 (a) 19x19 dot-matrix pattern (b) Pattern being projected onto the weld pool surface.....	21
Figure 2-8 High speed camera.....	22
Figure 2-9 Acquired reflected image by using dot-matrix pattern.....	23
Figure 2-10 Illustration for two kinds of corresponding	

relationships [6].....	24
Figure 2-11 Procedures of reflected image processing [6].....	25
Figure 2-12 Illustration of correspondence relationship between projected and reflected dots.....	26
Figure 3-1 Different Welding Directions [6].....	27
Figure 3-2 Reflected Images obtained using different welding directions.....	28
Figure 3-3 Block Diagram of the Whole Image Processing Scheme.....	29
Figure 3-4 Details at each stage of “feature extraction”.....	30
Figure 3-5 Flowchart of “feature extraction”.....	32
Figure 4-1 Acquired Reflected images using negative y-axis as welding direction.....	34
Figure 4-2 Preprocessing stage Block diagram.....	34
Figure 4-3 (a) Segmentation without preprocessing (b) with Preprocessing.....	35
Figure 4-4 Segmentation without DC level shift and with DC level shift.....	35
Figure 4-5 Subband coding.....	38
Figure 4-6 Result of 2D DWT of an image.....	39
Figure 4-7 A sample reflected image is wavelet transformed using “sym6” wavelet at level two decomposition.....	40
Figure 4-8 Various stages of Image preprocessing.....	42
Figure 4-9 Processing in Wavelet domain.....	43
Figure 4-10 (a) After Canny edge detection (b) after removing noise and axis and filling the holes.....	45
Figure 4-11 After Chow and Kanenko approach of adaptive Thresholding.....	47
Figure 4-12 After thresholding using (a) mean (b) median as the statistical operator.....	48
Figure 4-13 (a) After local adaptive thresholding using motion filter to convolve and a constant value of 0.01 (b) After median filtering (c) After removing vertical axis (d) After fixing	

broken dots by dilation and erosion.....	49
Figure 4-14 Binary Image where a dot is represented by a single pixel value of '1'	50
Figure 5-1 Flowchart of the Algorithm.....	51
Figure 5-2 Reflected image incorrectly dilated.....	53
Figure 5-3 (a) Structuring element used to dilate the left half of the convex shaped dot pattern (b) Structuring element used to dilate the right half of the convex shaped dot pattern.....	54
Figure 5-4 Final binary image dilated using special matrices.....	55
Figure 5-5 Dilated Images.....	56
Figure 5-6 (a) Structuring element B "rolling" along the inner boundary of A (the dot indicates the origin of B). (b) The heavy line is the outer boundary of the opening, (c) Complete opening.....	57
Figure 5-7 (a) Multiplied with (b) will result in (c). Dots in (b) and (c) are enlarged for better viewing in the document. In the actual case, a dot is represented by a single pixel value.....	58
Figure 5-8 The first dot of each row is marked with its pixel info and row number.....	61
Figure 5-9 The highest positioned point of each row is marked.....	62
Figure 5-10 Image showing the row with the missing dot.....	65
Figure 5-11 A color coded Binary image with the correct row numbers but localized column numbers.....	69
Figure 5-12 A color coded Binary image with the correct row and column numbers and missing dot number.....	70
Figure 5-13 Binary image showing the reference dot and the line connecting the corresponding dots in the remaining rows.....	71
Figure 5-14 (a) Original Image (b) Binary Image after segmentation (c) Result of position analysis (the resulting matrix of row and column numbers is depicted on the image.....	75
Figure 5-15 (a) Original Image (b) Binary Image after segmentation (c) Result of position analysis.....	76

Figure 5-16 (a) Original Image (b) Binary Image after segmentation	
(c) Result of position analysis.....	77
Figure 5-17 (a) Original Image (b) Binary Image after segmentation	
(c) Result of position analysis.....	78
Figure 5-18 (a) Original Image (b) Binary Image after segmentation	
(c) Result of position analysis.....	79
Figure 5-19 (a) Original Image (b) Binary Image after segmentation	
(c) Result of position analysis.....	80
Figure 5-20 (a) Original Image (b) Binary Image after segmentation	
(c) Result of position analysis.....	81
Figure 5-21 (a) Original Image (b) Binary Image after segmentation	
(c) Result of position analysis.....	82
Figure 5-22 (a) Original Image (b) Binary Image after segmentation	
(c) Result of position analysis.....	83
Figure 5-23 (a) Original Image (b) Binary Image after segmentation	
(c) Result of position analysis.....	84
Figure 5-24 (a) Original Image (b) Binary Image after segmentation	
(c) Result of position analysis.....	85
Figure 5-25 (a) Original Image (b) Binary Image after segmentation	
(c) Result of position analysis.....	86
Figure 5-26 (a) Original Image (b) Binary Image after segmentation	
(c) Result of position analysis.....	87

LIST OF FILES

Aparna_J.pdf2206KB

CHAPTER 1

INTRODUCTION

Welding is a fabrication process that is used to join two materials by melting and adding a filler material to form a weld puddle that cools to become a strong joint. It is a labor intensive process that requires great skill. Automation of this process will result in reduction of costs, consistent quality welds, improved capacity, higher productivity and repeatability. Though the existing welding robots help improve weld productivity, they lack the intelligent capabilities that human welders possess to achieve good quality of welds through observation of the welding process. Various techniques (including acoustic emission sensing technique, thermal sensing technique and vision based sensing techniques [1][2][3][4]) have been developed in the recent past in an effort to build intelligent next generation welding machines that emulate the skilled human welder.

1.1 Overview of GTAW

Gas tungsten arc welding (GTAW) or tungsten inert gas (TIG) welding, the process that is under test in this thesis, is a “manual” welding process that uses a non-consumable tungsten electrode, an inert or semi-inert gas mixture, and a separate filler material. This method is most often applied to stainless steel, light metals especially nonferrous metals and used when “quality welds” is extremely important (due of its capability of precision control of the fusion process [11]), such as in bicycle, aircraft and naval applications. But it requires significant operator skill and can only be accomplished at relatively low speeds. [5]

The general procedure of GTAW is as follows. Two pieces of metal are placed side by side and the welding torch is set above the seam. Then during the welding process, either the torch or work piece will be moved along the seam at a certain speed and the high-temperature welding arc under a certain current will melt the metal along the seam. Finally, the two work pieces are joined together shortly after cooling down. The quality of the weld depends on the important factor, the penetration depth. The extent of penetration can be decided by the top-side and back-side bead widths, which can be measured or deduced by the shape of weld pool surface during welding process [12].

From Figure 1-1, it can be seen that different shapes of weld pool surface are associated with different welding situations, and depend on different weld metals and welding parameters. Full penetration is desirable though partial penetration may be allowed to avoid burn-through. However, over penetration should be avoided as it will damage the material properties. [17]

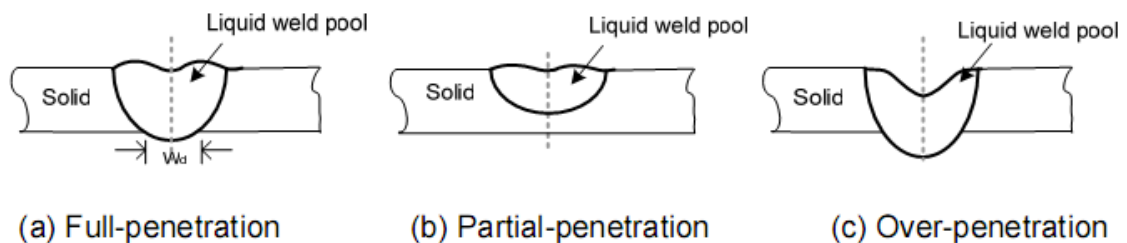


Figure 1-1 Different penetration statuses (profiles) in the welding process [6] [13]

Also, the human welder observes the weld pool surface to achieve quality welding or full penetration. Thus it can be deduced that if the surface of the weld pool is sensed, measured and reconstructed, the quality of weld may be known. Also parameters that can be used as feedback to control the welding process

can be derived from the reconstructed weld pool surface. In this chapter, various techniques used to sense a weld pool surface are discussed along with their benefits and limitations.

1.2 X-ray Radiation

A research based on radiography was conducted at the Ohio State University by Rokhlin and Guu [14]. The conclusion was that the penetration depth and pool depression are closely related and hence the weld depression can be used for controlling weld penetration. But, since the principle behind this method is to measure the material thickness, for full penetration where backside pool surface deformation occurs, the pool surface shape will be difficult to extract. [6]

1.3 Ultrasonic Technique

Another way to measure the depth of penetration of a weld pool is to locate the fusion interface between the weld pool and parent metal using ultrasonic waves. The ultrasonic wave is generated by an angled piezoelectric transducer in contact with the surface, as shown in Figure 1-2. As can be seen, the deeper the weld pool, the shorter the total beam path. [15]

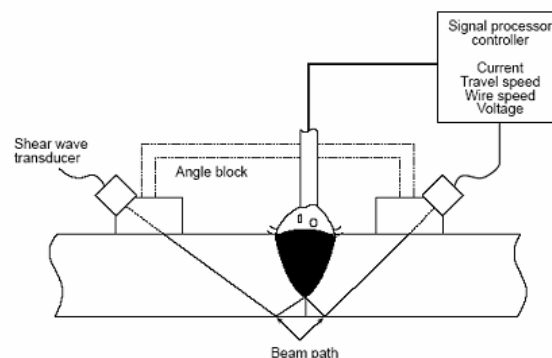


Figure 1-2 Ultrasonic penetration sensing system [15] [6]

But, for this technique to be effective the work piece must have a simple, uniform surface with minimum irregularities to ensure good coupling between the work piece and the transducer. Also, since the transducers must track the weld pool, component vibration or unexpected probe movement must be prevented during the process.

1.4 Weld Pool Sag Sensing Method

When full penetration is achieved in the welding process, the weld pool surface begins to sag towards the back of the plate because of the arc pressure and gravity. This characteristic is utilized in weld pool sag sensing method [40]. The sag movement can be detected through the increase in arc length, or the change in profile of the weld pool. But, the magnitude of the sag movement is very small and this limits the accuracy attainable. The accuracy is reduced by the increase of the work piece thickness, and by weld pool oscillations due to pulsed welding current, addition of filler wire and other unstable factors. Thus weld pool sag sensing method is limited to butt welds in the flat position and requires a highly accurate power source. [16]

1.5 Acoustic Emission Sensing Technique

During the welding process, the stresses due to the thermal gradient of the weld and change of the fused metal volume generate acoustic emissions. The acoustic emissions travel throughout the work piece and can be detected. As penetration changes from partial to full, the frequency spectrum of the acoustic emission changes. A stationary acoustic transducer remote from the weld can be used to measure the emission. Also for laser welding, a non-contact pressure

wave sensor is applied. But, the relationship between the acoustic emissions and the weld penetration depth is not fully understood and some micro-structural features may also influence the performance. [17] [6]

1.6 Thermal Sensing Technique

Thermal sensing technique assumes that if the thermal gradient around the weld is constant, then the weld pool penetration is constant. And in this method the temperature may be measured using a contact thermocouple or an infrared pyrometer or a camera. Although thermal sensing is the most widely applied technology in practical use and also provides seam tracking, this system is particularly sensitive to variations in the surface condition and the emissivity of the material. The accuracy of camera-based systems is reduced by contributions from the arc light and this can be greatly overcome by the use of filters. [18] [6]

1.7 Weld Pool Oscillation Sensing

In pulsed welding processes, the surface of the pool vibrates. Some researches show that the oscillation frequency is dependent on the weld pool size, and is higher in partial penetration than in full penetration. And the oscillation frequency can be monitored by measuring the fluctuations of either the arc voltage or the arc light reflection. But, the accuracy of the method is reduced as the travel speed increases. It is also reduced due to the power source ripple, presence of dirt, slag or oxide at the back of the weld pool and the addition of filler wire to the weld pool. Hence weld pool oscillation frequency monitoring by optical systems can only be used for full penetration butt welds, and requires the back surface of the weld to be free of oxide and contamination. [19] [6]

1.8 Vision Based Sensing

Among the existing methods, the vision based sensing techniques received considerable amount of attention. The human welder uses vision to observe the weld pool surface to decide the quality of the weld (or the penetration depth) and to adjust the parameters such as weld current and speed. To automate this process using machine vision, vision based sensors and computer algorithms are used. The sensors or the cameras try to “see” by capturing images of the weld pool surface, examining each pixel in the images, processing them and attempting to develop conclusions with the assistance of knowledge bases and pattern recognition engines. They are also used to extract weld pool related parameters to be used as feedback by the control systems to adjust welding parameters [6][7][8][9].

1.8.1 Two-dimensional Observation and Analysis

The 2D geometric parameters, such as the length, width and area, are used to develop a model to predict the penetration of the weld work pieces. A monochrome or color camera with a band-pass filter is used to acquire weld pool images. The experimental setup and an acquired image are shown in Figure 1-3.

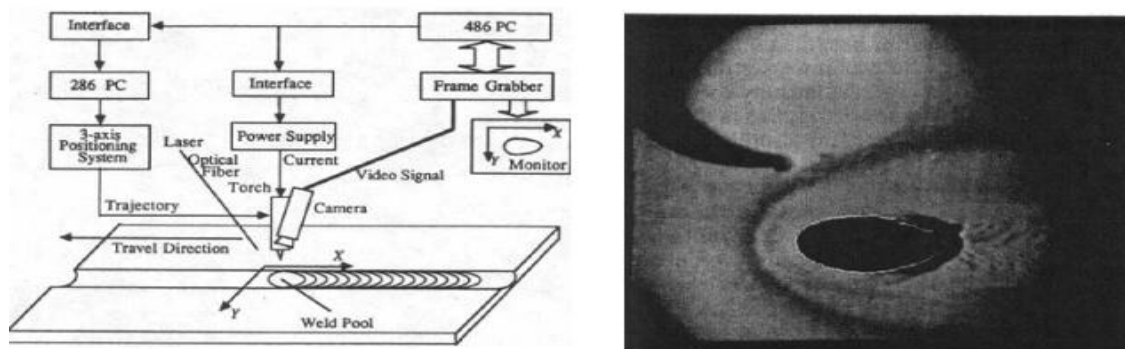


Figure 1-3 Experimental set up and the acquired image [7] [6]

Work was done earlier in the University of Kentucky [7] by using the laser strobe system. The weld pool is observed at an angle to the welding direction. Since the camera is synchronized with the pulsed laser, the laser power density during 'on' duration is much higher than welding arc and clear images of weld pool surface can be captured as shown in Figure 1-3. On-line weld pool edge extraction is done based on the grayness difference and its directional gradient among the weld pool, the heat affected zone (HAZ) and the base metal. Various experiments have been performed by using different system parameters. The experimental results verified the controller could maintain the pool size closer to the desired level with the variations in the system.

Another important technique for a 2D weld pool boundary measurement is the co-axial viewing of the weld pool. It was first proposed by Richardson et al [20]. It has been widely investigated by some researchers. In the co-axial viewing method, an electrode is used to block the arc.

The two-dimensional size (length and width) of the weld pool is determined by using the calibration transformation of 0.043mm/pixel. Figure 2-4 and Figure 2-5 show some of the images captured, the result of the image processing, and the extracted shape of the weld pool [21]. The research performed had practical implementations in the industry since the equipment used was cheap, and was based on passive sensing (no laser). However the measurement was only two-dimensional and the state of the weld pool penetration cannot be precisely determined by it.

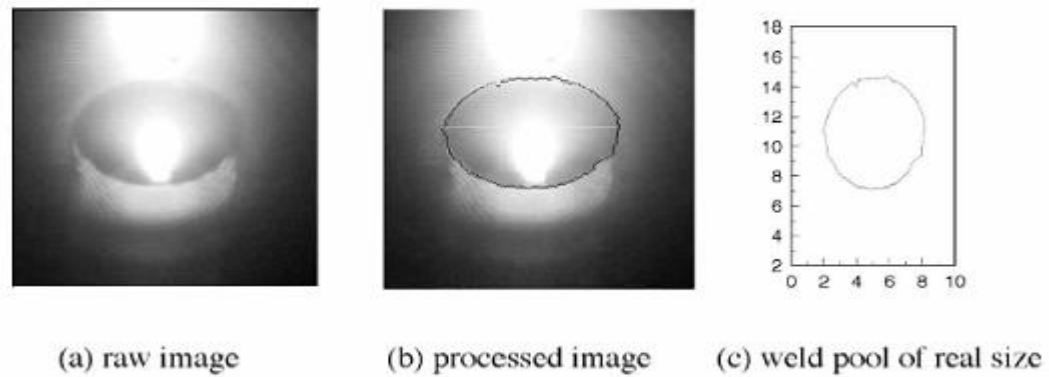


Figure 1-4. Weld pool geometry at current of 90 A and speed of 103mm/s [21] [6]

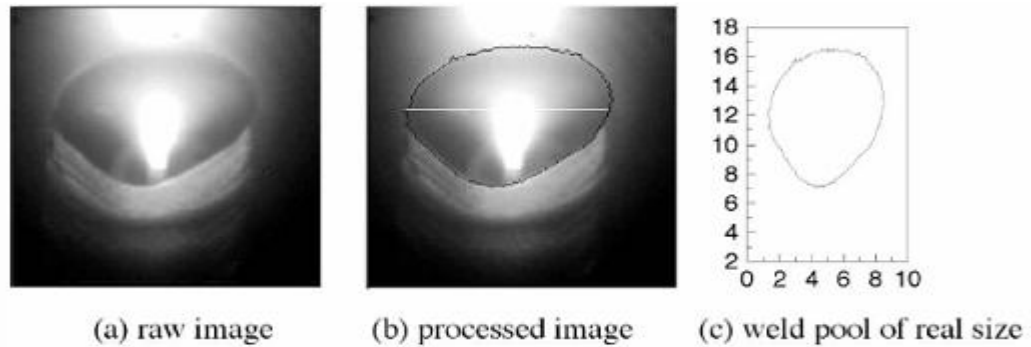


Figure 1-5 Weld pool geometry at current of 100 A and speed of 113mm/s [21]

[6]

1.8.2 Three-dimensional Observation and Analysis

Three-dimensional (3D) observations/measurements provide more insight on the state of the weld pool by adding another dimension, the depth of depression, to the measurement. More detailed information about the condition of the weld pool can also be determined in 3D measurement experiments. For 3D analysis, many techniques such as stereovision, biprism and structured light have been used to determine the depth of the weld pool experimentally [22].

The first true 3D observation method for the weld pool surface was developed at Welding Research Laboratory, University of Kentucky (UK) based on two major

advances [8]. First, to eliminate the influence of the bright arc light, a short duration pulsed laser was projected onto the weld pool and the camera shutter was synchronized with the pulse duration. The arc light was essentially eliminated from the image when the shutter speed was fast enough. Second, a special technique [8] [6] was proposed in order to acquire information from the specular surface. In fact, common practice for measuring a surface is to project a structured light onto the surface and sense the diffuse reflection from the surface [23] [24] [25] [6]. Unfortunately, the specular nature of the weld pool surface poses a problem. The special technique proposed in [8] is to project the laser through a frosted glass so that the laser's travel direction changes because any point of the frosted glass becomes a new point light source which disperses light with a certain diffuse angle. The camera views the slits (grid openings) through their reflection from the weld pool surface. Their virtual image [26] consists of bright stripes deformed by the weld pool surface deformation and is sensed by the camera [8]. The resultant image contains the information about the shape of the weld pool surface.

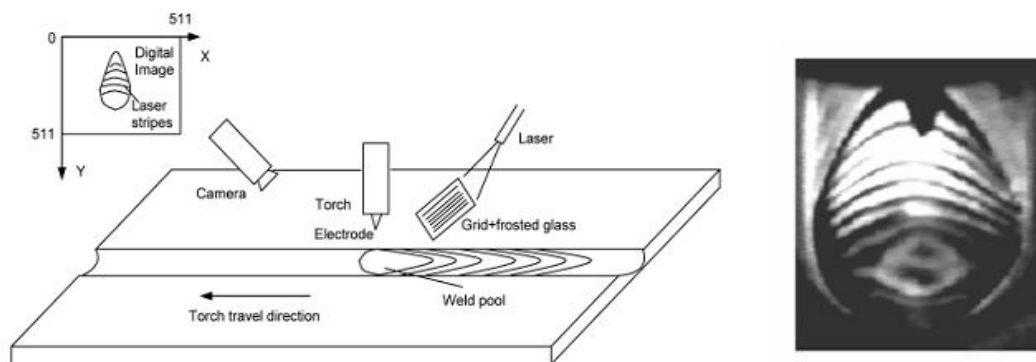


Figure 1-6 Experiment scheme and image acquired under high power pulsed
Laser [8] [6]

As can be seen in Figure 1-6, the above method is capable of obtaining specular reflection from the weld pool surface in the presence of the bright arc. However, the limitations of this technique are that the synchronization of the laser and high-speed shutter require specific, high cost and sophisticated equipment, which is not suitable for use in production. More critically, to suppress the arc, the power of the laser during the pulse must be very high (70 kW for images shown in Figure 1-6) and the frame rate thus cannot be very high (30 frames per second for images in Figure 1-6) because a high frame rate would increase the average power of the illumination laser.

As a solution to the problems posed by the previous methods, a better method was proposed in that used the specular nature of the weld pool to an advantage by capturing the reflected images instead of direct images of the surface.

Saeed, Lou and Zhang at the University of Kentucky have done some numerical simulations using slope field and point tracking techniques to compute the 3D shape of the weld pool surface [27]. In their method a 7x7 dot matrix pattern of laser is projected on the weld pool. The reflection of the dot matrix was observed on the imaging plane. On the basis of the geometry, law of reflection and using an approximation, the slope field of the surface was computed and an estimated weld pool surface is formed as shown in Figure 1-7. But, this simulation work is done only considering the simplified and ideal welding environment.

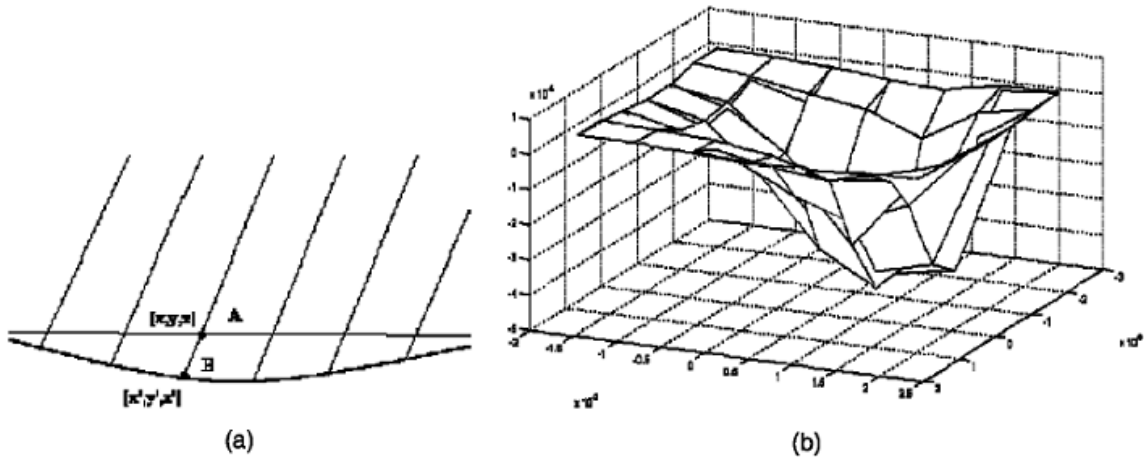


Figure 1-7 Simulation of 3D weld pool surface (a) Approximation of reflection point (b) Estimated weld pool surface from slope field [27] [6]

Later, Hongsheng Song, also at the University of Kentucky, worked on surface reconstruction of the weld pool using reflected images. He used a 19x19 dot-matrix pattern of structured laser light and a high speed camera to capture the specular reflection of the light pattern from the pool surface. One of the captured reflected images is shown in Figure 1-8 and the result of position analysis of the reflected dots is shown in Figure 1-9.

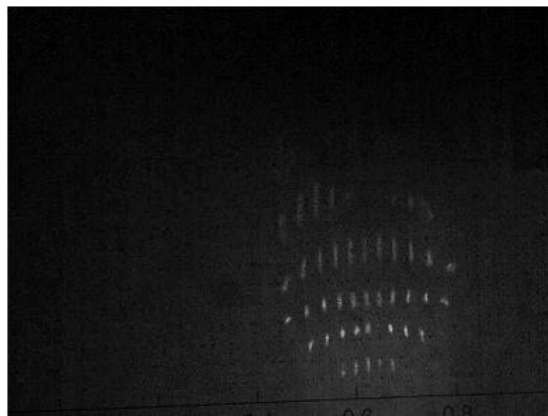


Figure 1-8 A captured reflected dot-matrix image [6]

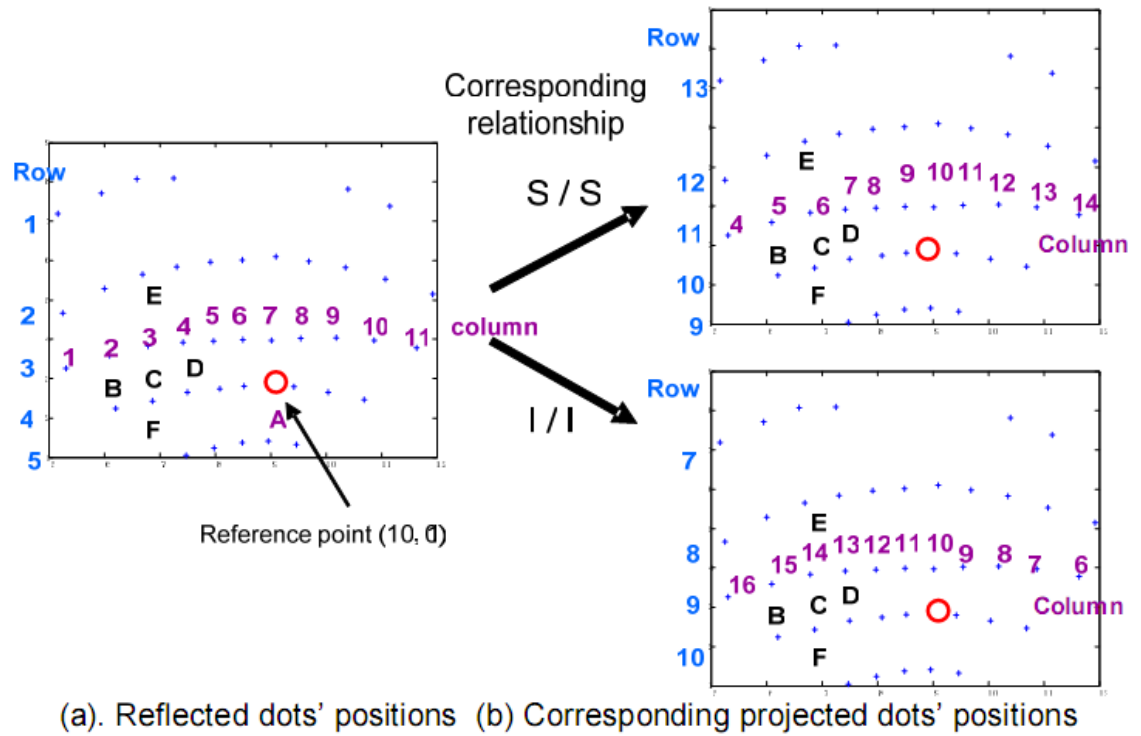


Figure 1-9 Illustration of correspondence relationship between projected and reflected dots

Although this proved to be better compared to earlier techniques, the accuracy of the weld pool surface measurement had to be improved (very less information about the surface is known since only a few dots reflected by the surface).

1.9 Thesis Objective

The objective of this thesis is to improve the vision-based method that uses specular reflections of the weld pool surface and implement an algorithm for processing the reflected images to find the positions of each dot in the reflected dot-matrix pattern. This information can later be used by a surface reconstruction algorithm to derive the three-dimensional weld pool surface. The improvement has been achieved by increasing the density of dots reflected as a result of choosing a different welding direction which in turn increases the amount of

information known about the weld pool surface. If welding direction cannot be changed in the experimental setup, the structured laser dot-matrix pattern can be made incident from the opposite direction. Both have similar effects on the reflected dot-matrix pattern.

This kind of processing of the reflected images allows us to observe the dynamic changes of the weld pool surface, analyze the impact of weld parameters during the process, deduce the penetration depth, an important factor used to decide the quality of the welding process, and to easily build a reconstruction algorithm based on the reflection law.

The proposed method is better compared its predecessors in terms of cost, convenience, robustness and accuracy. Better accuracy is due to increased density of the dots in the reflected dot-matrix pattern since more reflected dots would mean more information about the surface and hence reconstruction would be more accurate.

1.10 Thesis Outline

This chapter gave an overview of some of the existing techniques for weld pool surface measurement along with their limitations. It went on to explain the objective of the thesis which is to improve the vision based sensing technique.

The rest of the chapters in this thesis are organized as follows.

Chapter 2 presents a review of the vision based sensing technique that is being improved upon in this thesis. It gives a quick introduction to the experimental setup, the algorithm and the results. Though this method proved to be

successful, since it used the specular property of the weld pool surface to an advantage, its accuracy in reconstructing the surface had to be improved.

Chapter 3 introduces the cause for the improved accuracy of the proposed algorithm. The proposed algorithm increases density of reflected dots which further results in improved accuracy. This increased density is achieved by choosing a different welding direction. At the end, the chapter gives an overview of the proposed algorithm in the form of block diagram and flowcharts.

Chapter 4 explains in detail the feature extraction part of the algorithm. This includes the preprocessing stage (or the noise removal stage) and the image segmentation stage. The technique used to remove noise in the reflected images is based on wavelet transform. Local adaptive thresholding is used to segment the preprocessed image.

Chapter 5 deals with the position analysis of the segmented dots. It explains the morphological processing techniques used to extract the position of each dot in the binary image. At the end, it gives the results of the proposed algorithm when applied to various test images.

Chapter 6 concludes the thesis discussing the main contributions made along with the future work of this project.

The software used for implementing the proposed algorithm is MATLAB 7.3.0(R2006b).

CHAPTER 2

SYSTEM REVIEW

This chapter intends to provide an overview of the technique that is being improved. It needs to be reviewed first since it forms the basis for this thesis. The main disadvantage of the earlier methods for surface measurement is the specular property of the weld pool surface. As a solution, a method was initially proposed in [6] which uses the specular property of the surface to an advantage. Instead of capturing direct images of the structured light pattern on the pool surface, its reflection is captured.

In physics, reflection is defined as the change in direction of a wavefront at an interface between two dissimilar media such that the wavefront returns into its originating medium. Common examples include the reflection of light, sound and water waves. Reflection of light may be diffuse (not retaining the image, only the energy) or specular (mirror-like) depending on the nature of the interface.

2.1 Diffuse Reflection

When light strikes a rough or coarse surface, it bounces off in all directions due to the microscopic irregularities of the interface. This is called diffuse reflection as shown in Figure 2-1.

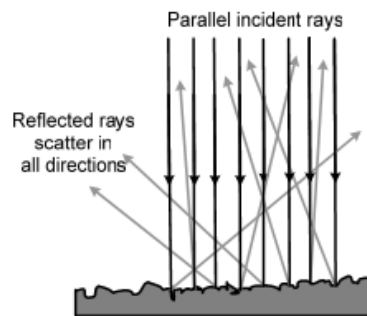


Figure 2-1 Diffuse reflection [6]

2.2 Specular Reflection

Specular reflection is the perfect, mirror-like reflection of light from a surface where a single reflected light ray results from a single incident light ray. Such behavior is described by the reflection law, which states that the reflected light ray and the incident light ray make the same angle with respect to the surface normal. The reflection law is commonly stated as $i = r$, just as shown in Figure 2-2.

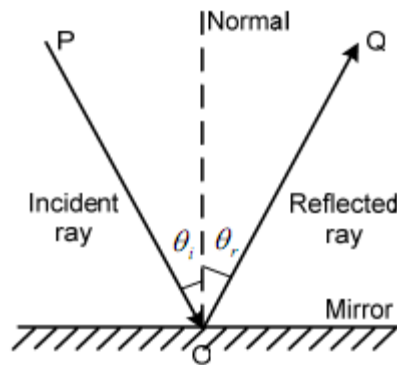


Figure 2-2 Specular reflection [6]

Even when a surface has specular property (i.e. no diffuse reflection), not all the incident light is necessarily reflected. Some of the light may be absorbed by the surface material or transmitted through the surface. For most interfaces between materials, the fraction of the light that is reflected increases with increasing angle of incidence i . If the light is propagating in a material with a higher index of refraction than the material whose surface it strikes, then total internal reflection may occur.

Thus, the specular nature of the weld pool surface is turned into an advantage in the system proposed by Hongsheng in [6] by capturing the specular reflection of

the projected laser light pattern on the weld pool surface. The arc light intensity decreases with the square of the distance. However due to the coherent and unidirectional property of the laser light waves, the laser's travel direction remains unchanged and its intensity or power loss over the distance traveled by the laser light is insignificant in comparison with that of the arc. In addition, the specular surface of the weld pool reflects nearly all the intensity of the projected illumination laser lines. Hence, if the imaging plane is placed reasonably far from the torch, the intensity of the laser light falling on it will be much stronger than that of the arc light. Hence, it is possible to obtain the reflection of the projected laser clearly on an imaging or interception plane. Thus, the resulting “reflected image” on the imaging plane is captured by a high speed camera.

Initially, a multiple line pattern was projected on to the weld pool surface. The pattern and its application in the system are shown in Figure 2-3. One of the captured reflected pattern images is shown in Figure 2-4.

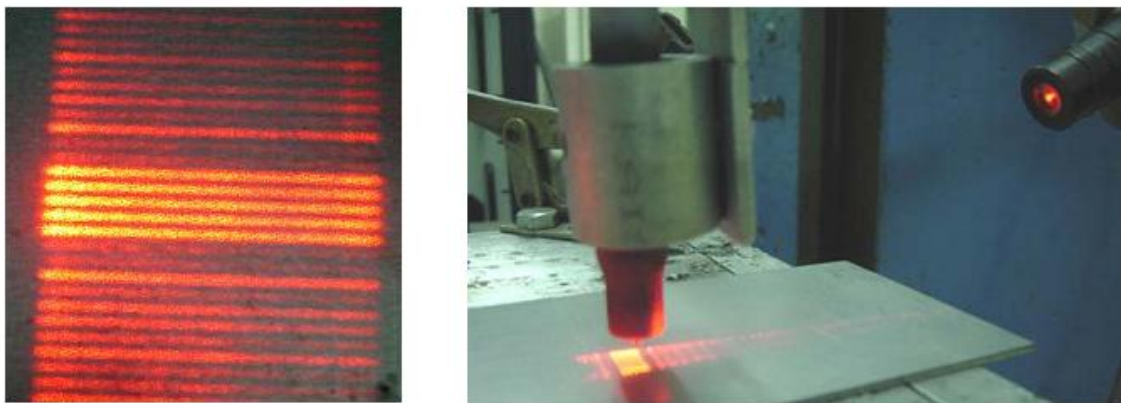


Figure 2-3 Multiple-line pattern and its application in the system [6]

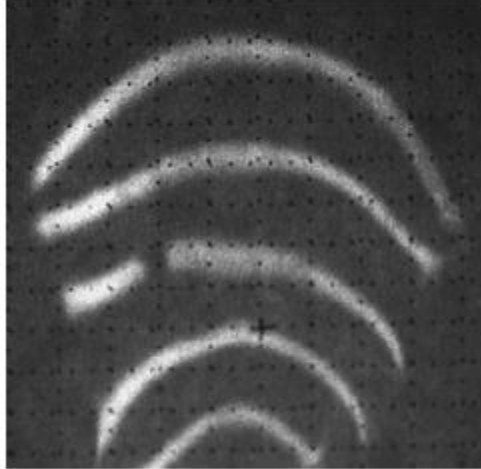


Figure 2-4 Image of reflected Laser Line pattern on a mild steel work piece. [6]

Though clear reflected images can be achieved by using multiple-line pattern of structured light, and the images contain 3D information of the weld pool surface, these images with reflected lines are difficult to be used for reconstruction of the weld pool surface based on reflection law. Hence after considering many options, a SNF laser with a 19-by-19 dot matrix pattern lens whose projection area can cover the whole weld pool area with reasonable close distance between dots was used.

2.3 Experimental Setup

The experimental setup (as shown in Figure 2-5) for acquiring the reflected images can be summarized as follows. A structured laser dot-matrix pattern produced by a low-power illumination laser diode is projected onto the specular weld pool surface and the corresponding reflection is observed on an imaging plane whose image is captured by a high-speed camera with a narrow band pass filter. The arc radiation decays very fast with the distance traveled unlike the

reflection of the projected laser. Hence, it is possible to obtain the reflection of the projected laser clearly on the imaging or interception plane.

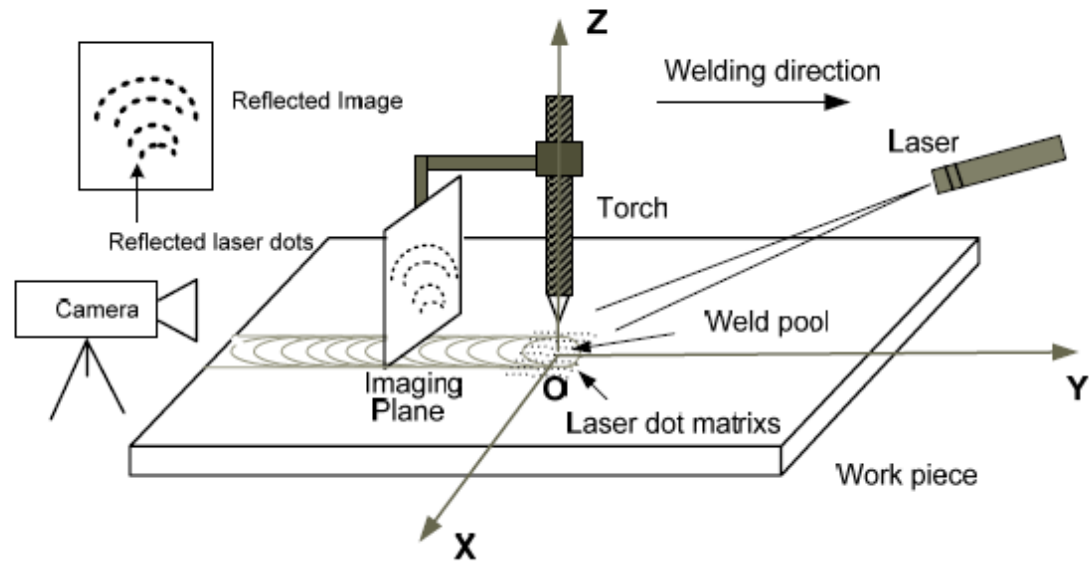


Fig. 2-5 Experimental setup for obtaining reflected images of the specular surface of GTAW pool [6]

The welding process used in this project is *Gas Tungsten Arc Welding (GTAW) without filler material*. A PULSEWELD gas tungsten arc welding (GTAW) machine with cooling system and shielding gas is used. The system parameters are interactional, and positioning simulation is needed to select/verify proper system parameters. In the proposed system, the height of the electrode can only be adjusted in a limited range (typically 3 ~ 5 mm in GTAW), thus the projected or reflected laser rays would be blocked by the electrode if the position or angle of laser diode is not appropriate. Even if all the laser lights projected onto the weld pool surface are not blocked, the position and size of the imaging plane decides whether all the reflected rays can be projected onto the imaging plane.

The major components used in this system are listed as follows:

1. Welding torch

The work piece is welded by keeping the torch stationary and moving the work piece at a certain speed. The welding current is kept at 70 Amp, and the welding speed is about 2 mm/s. The tungsten tip of the torch is placed at 3 mm from the work piece such that it does not block the reflected light pattern and welding arc is stable. The *welding direction* here refers not to the direction in which the welding torch moves, but to opposite direction in which the work piece moves.

2. Work piece

A 2 mm thick mild steel sheet is used as the work piece to be welded. A welded work piece is shown in Figure 2-6.

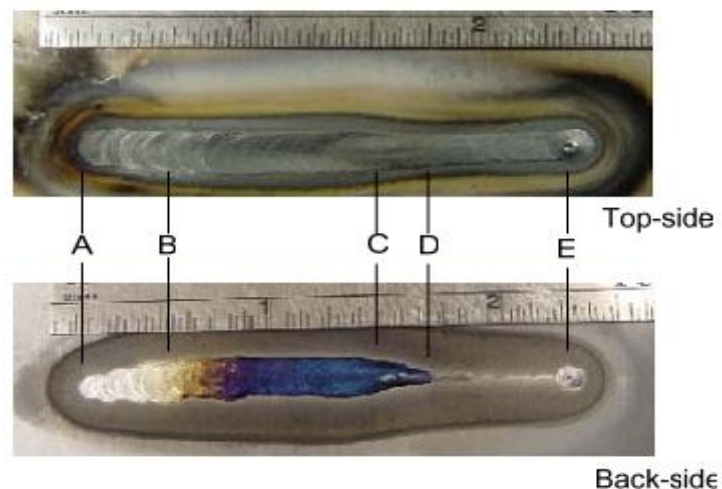


Figure 2-6 Welded Work piece [6]

3. A laser diode to produce structured laser light

A light pattern composed of a 19 x 19 dot matrix (about 0.5-1 mm distance between dots, 50 mm projection distance and 0.77 degree inter-beam angle) projected onto the surface of the weld pool at a particular angle by “StockerYale's Lasiris™ SNF uniform intensity” laser projector (wavelength: 685nm, power: 20mW) as shown in Figure 2-9. The diffractive lens used is Five-line pattern - fan angle: 5 degree, inter-beam angle: 0.23 degree.

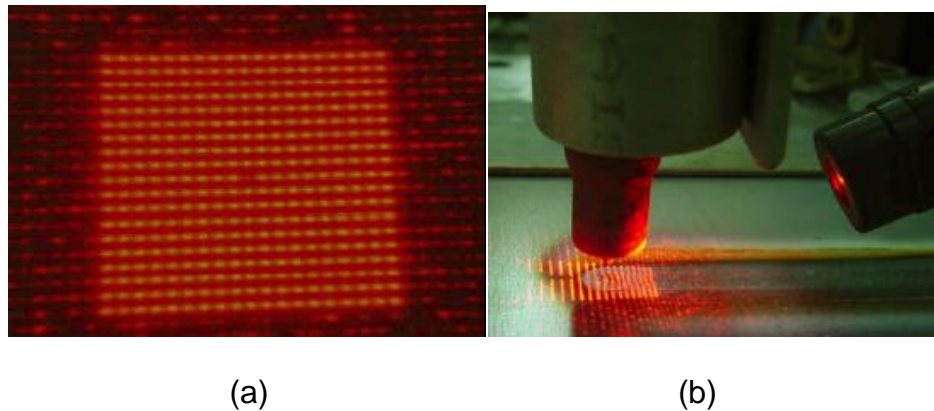


Figure 2-7 (a) 19x19 dot-matrix pattern (b) Pattern being projected onto the weld pool surface.

The dot right at the center of the 19 x 19 dot matrix pattern is made absent so that this missing dot can be used as a reference in finding the correspondence map between projected dots and reflected dots. Also, the projected pattern should cover the whole possible area of weld pool (about 8mm*10mm area) and the distance between the dots should be very small (about 0.5mm) in order to measure the weld pool surface precisely. This is ensured by placing the laser at the right distance from the work piece, approximately 40 mm. A 30 degrees laser projection angle is chosen such

that the reflected pattern is not blocked by the torch and most of the reflected light pattern is intercepted by the imaging plane. Also, the center dot is projected just below the torch (origin of the universal coordinate system) to make measurement easy.

4. Imaging plane

A piece of 4" x 4" square glass with a grid paper attached has been chosen as the imaging plane in this system. Reflection is intercepted on one side and image is captured from the opposite side. Hence, glass is chosen due to its transparency. Glass also helps prevent the grid paper from burning due to the high temperature of the welding arc.

5. Camera to capture the reflection from the imaging plane

To reduce the cost and complexity of the system, smart cameras with in-built embedded processors are increasingly being used. They also eliminate the need for a separate frame grabber card. The camera used in this system, Olympus *i-SPEED*, is also a smart high-speed monochrome camera with a band-pass filter (lens). It is placed 1~2 meters away from the imaging plane.



Figure 2-8 High speed camera

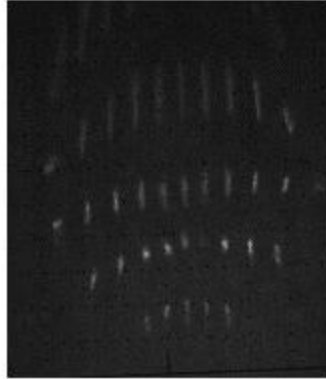


Figure 2-9 Acquired reflected image by using dot-matrix pattern

The acquired reflected image (as shown in Figure 2-9) then needs to be processed by specialized image processing algorithms to find a correspondence map between the projected and reflected dots to determine which dot on the reflected image corresponds to which dot on the projected dot matrix pattern.

This correspondence map is later used to reconstruct the weld pool surface.

There are two kinds of corresponding maps/relationships, namely column and row correspondence maps. Column correspondence gives the column relationship between the dots in a particular projected row and its reflected row. Row correspondence tells the row relationship between the dots in a particular projected column and its reflected column. These relationships have three types of mapping according to different shapes of reflection surface: sequential, inverse and disordered as shown in Figure 2-10.

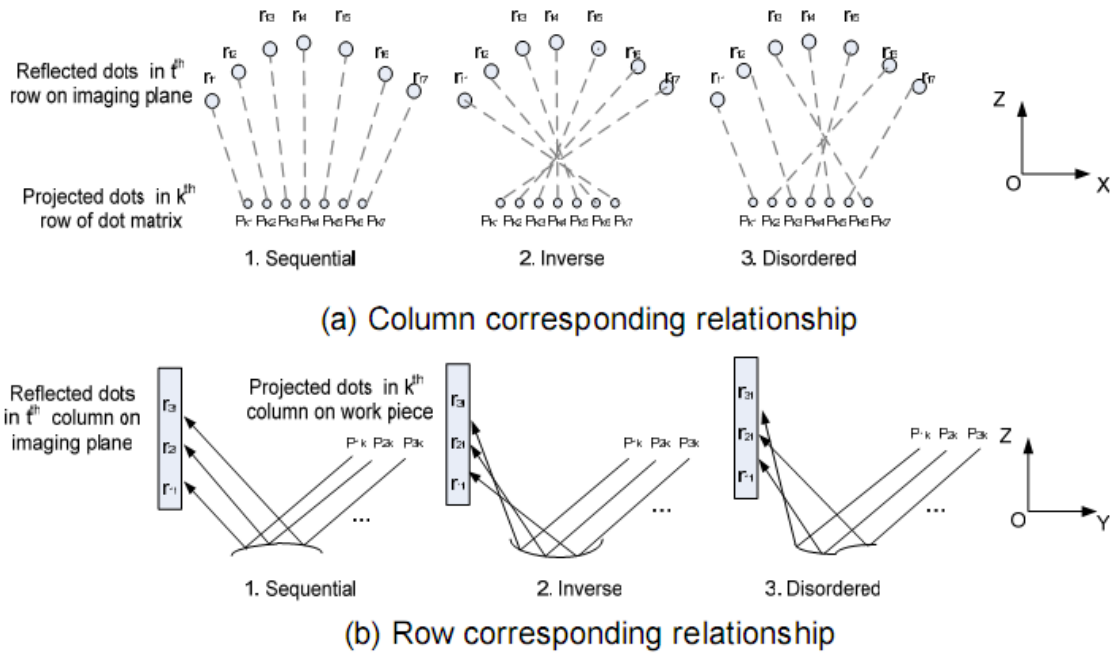


Figure 2-10 Illustration for two kinds of corresponding relationships [6]

Correspondence simulations were used to find the possible relationships between projected and reflected laser rays. The simulation results show that for most simulated concave and convex surfaces, the shape of the reflected dots in a row is convex. The row and column corresponding relationships are 'Inverse' for concave surfaces while they are sequential for convex surfaces.

2.4 Algorithm and Results

The reflected image processing algorithm used is shown in the form of a flowchart in Figure 2-11.

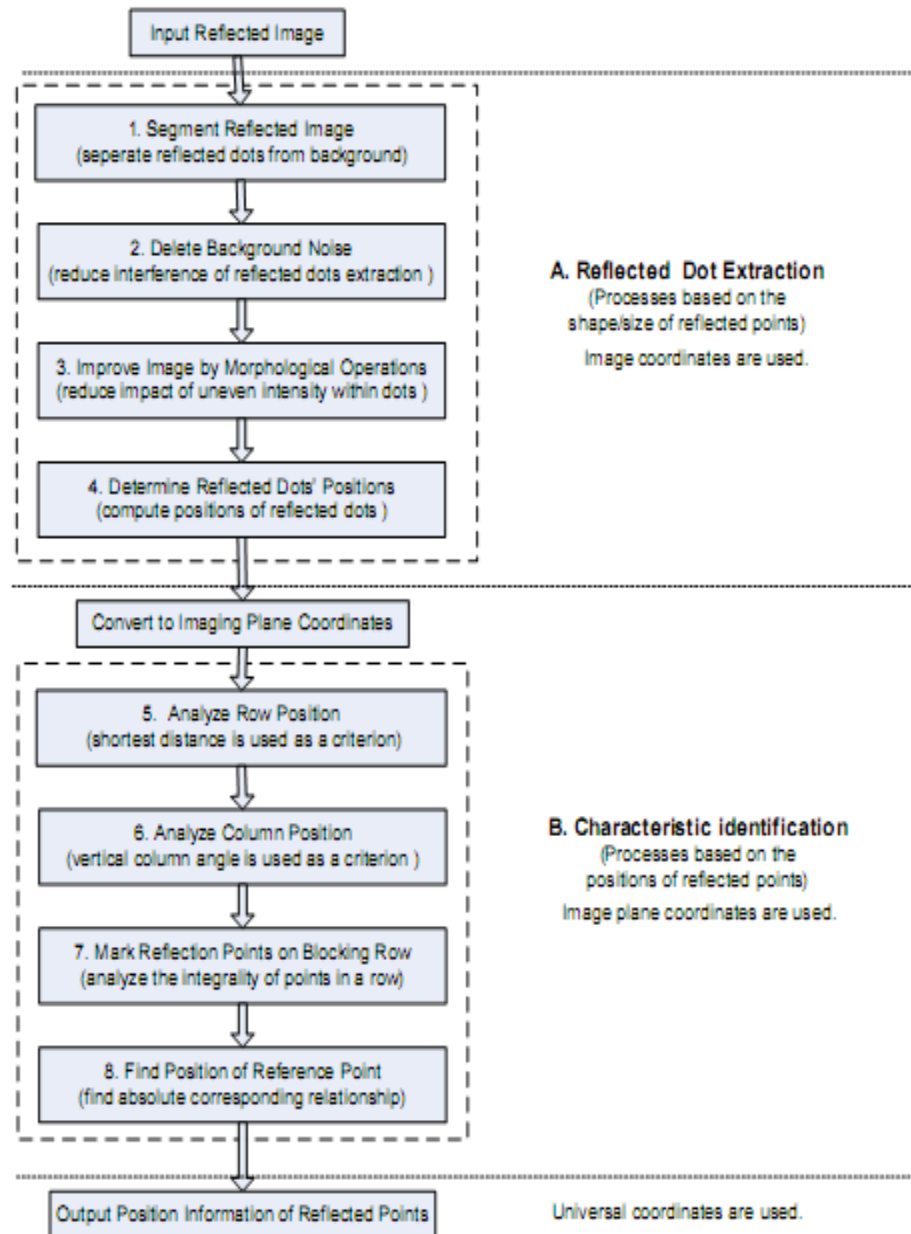


Figure 2-11 Procedures of reflected image processing [6]

The result of applying this algorithm to the acquired image is shown in Figure 2-12.

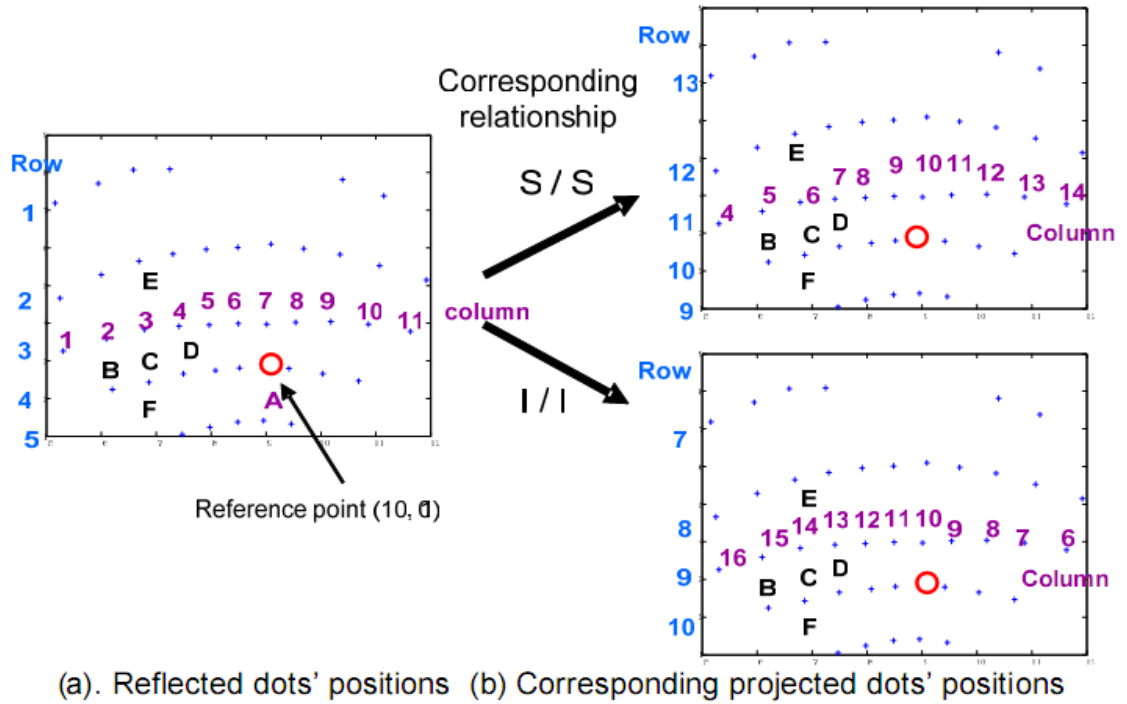


Figure 2-12 Illustration of correspondence relationship between projected and reflected dots

Thus, this method not only converts the disadvantage of the previous method to an advantage, it also uses the reflection law to easily reconstruct the weld pool surface. Although this method proves to be successful, it does not give a very accurate measurement of the weld pool surface. This is due to the fact that very few dots are made incident on the surface and thus less information is available for reconstruction. The accuracy may be improved if greater number of dots is projected onto the weld pool surface. But greater density of dots in the reflected dot matrix pattern will demand a complicated image processing algorithm for reflected image processing. This thesis describes an improved reflected image processing algorithm and a better method to find the row and column positions of the dots in the reflected image.

CHAPTER 3

IMPROVEMENT OF THE SYSTEM

Improvement is achieved by increasing the density of the reflected dot-matrix pattern by choosing the welding direction opposite to the one in the existing technique. This is equivalent to projecting the structured laser light pattern in the opposite direction.

In this experiment, the welding direction refers to the opposite direction in which the work piece moves during the welding since the torch is stationary. The welding direction chosen has an effect on the resulting reflected laser light (dot-matrix) pattern and in turn affects the accuracy of surface measurement.

Two practical situations with different welding directions have been illustrated in the Figure 3-1.

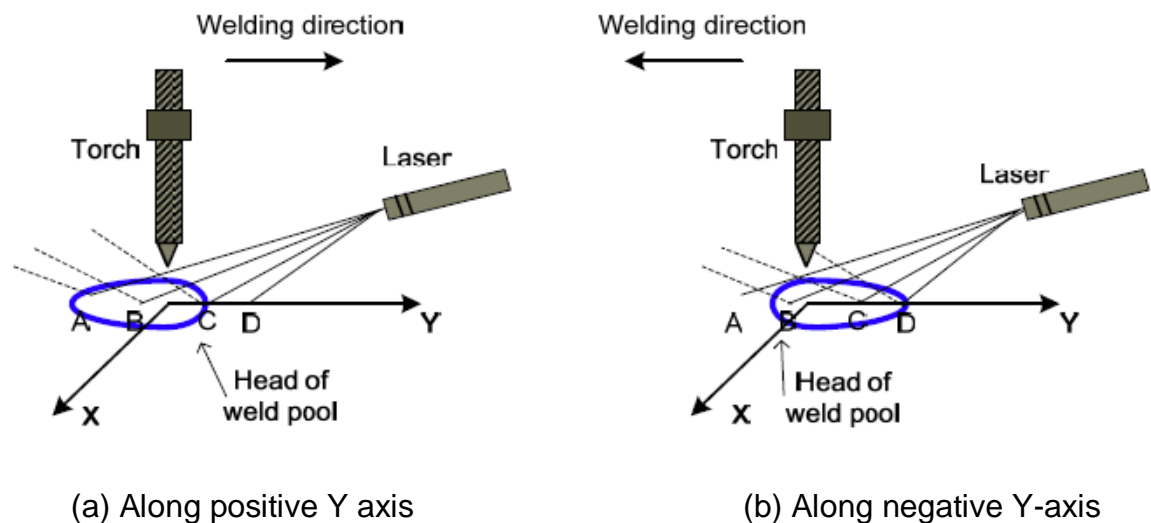
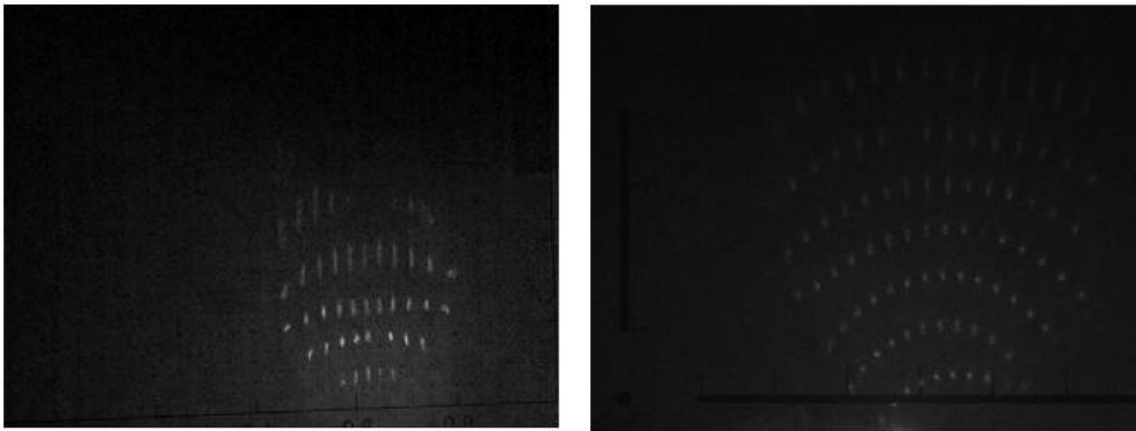


Figure 3-1 Different Welding Directions [6]

As can be observed from the Figure 3-1, the head of the weld pool is along the welding direction and is nearer to the tungsten electrode or torch. Consider four

incident light rays namely A, B, C, D. In Figure 3-1(a), light rays A, B and C fall on the weld pool surface and are reflected onto the imaging plane without getting blocked by the torch due to the 3~5 mm height of tungsten electrode and 30 degree laser projection angle. In Figure 3-1(b), light rays B, C and D fall on the weld pool surface and only B and C get reflected onto the imaging plane successfully. D may get blocked by the torch since its distance to the torch is large and the height of the torch is only 3~5 mm. This implies that welding direction along positive Y-axis will lead to good reflected images with few light rays getting blocked.

But, this welding direction will result in only a few dots getting reflected by the weld pool surface as opposed to the number of dots that get reflected if the welding direction is along the negative Y-axis. This is illustrated in Figure 3-2.



(a) Welding direction along negative Y-axis (b) Along positive Y-axis

Figure 3-2 Reflected Images obtained using different welding directions.

Greater density of dots on the reflected dot matrix pattern implies that more information about the surface of the weld pool is available. Due to the change in the welding direction, larger number of dots falls on the surface and gets

reflected onto the imaging plane though a few of them get blocked by the torch. In other words, the same surface is getting covered by greater number of dots. Detailed information of the surface is now available and thus accuracy of measurement increases.

Hence, the welding direction is chosen along negative Y-axis. The increased accuracy of measurement of the three-dimensional weld pool surface increases the complexity of the image processing algorithms for determining the position of each dot on the reflected dot-matrix pattern increases. Thus position analysis is now a more challenging problem and thus better methods have been proposed and implemented. The basic block diagram of the improved image processing scheme used to do the position analysis of the weld pool reflected dot matrix pattern image is as shown in Figure 3-3.



Figure 3-3 Block Diagram of the Whole Image Processing Scheme

The experimental setup for acquiring images remains the same except for the different welding direction. As shown in the Figure 3-3, the acquired reflected images are to be processed by suitable image processing algorithms in order to extract the position (row and column numbers) of each dot in the reflected dot-matrix pattern. This information can later be used to find a correspondence map between the reflected dots and projected dots which in turn can be used to reconstruct the surface of the weld pool. The surface reconstruction part has

been done by Hongsheng Song [6]. This thesis implemented the algorithms to perform the feature (reflected dots are the features being extracted) extraction and position analysis of the dots in the acquired images. The details at each stage of feature extraction are shown in Figure 3-4.

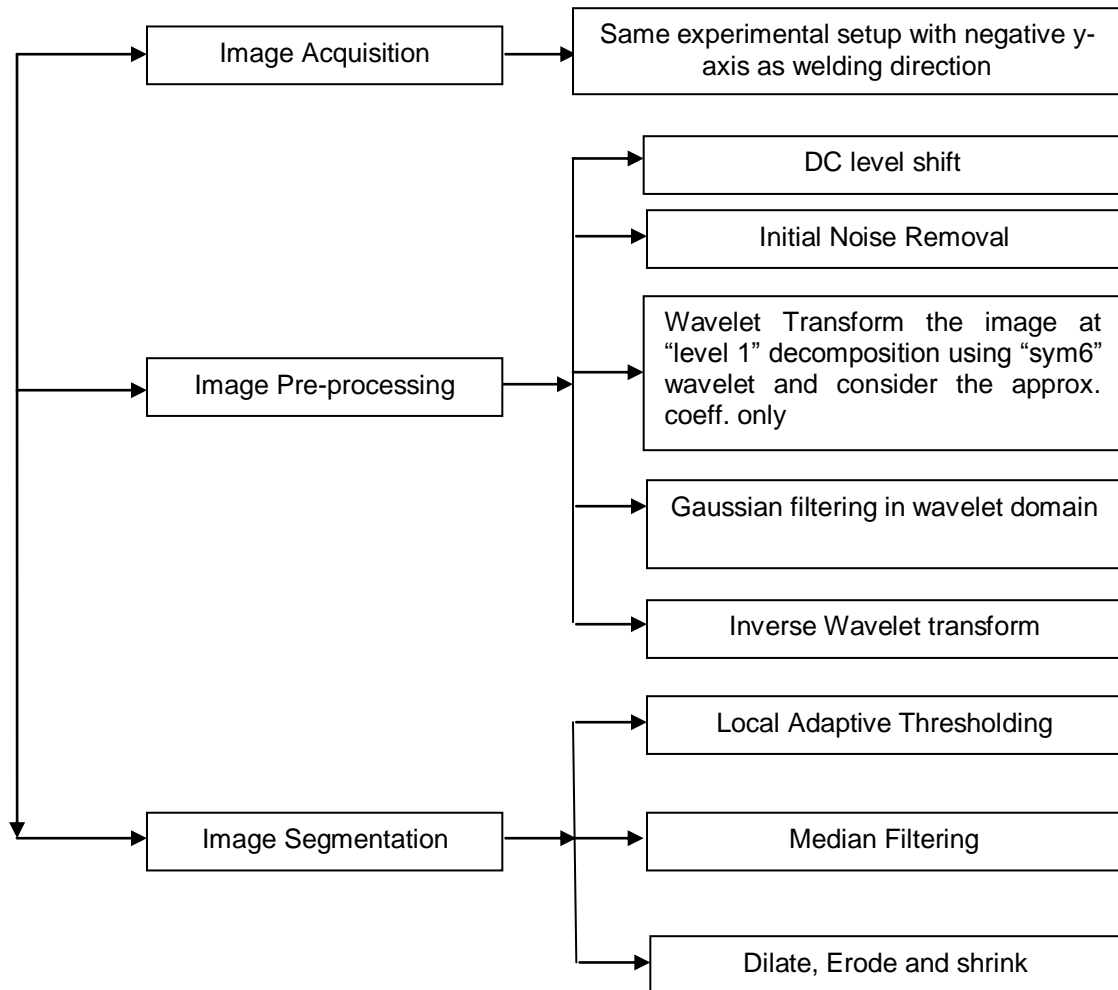


Figure 3-4 Details at each stage of “feature extraction”

As shown in Figure 3-4, the techniques used to segment the image are quite different from those used in its predecessor. Before actual segmentation is done, noise introduced in the image acquisition stage should be removed. This is taken care of in the “Image Pre-processing” stage. Denoising based on wavelet

transform proved to be an effective technique for the reflected images under consideration. In the “Image segmentation stage”, the best method was found to be “Local adaptive thresholding”. It had to be followed by median filtering (to remove the salt and pepper noise) and “dilation, erosion” to remove any leftover noise. Shrink reduces the dots to single pixel values such that in the binary image, a pixel value of ‘1’ would indicate the presence of a dot while a ‘0’ would mean background. This binary image is ready to be sent to the position extraction stage. The details at “position extraction” stage are given in the form of a flowchart below in Figure 3-5.

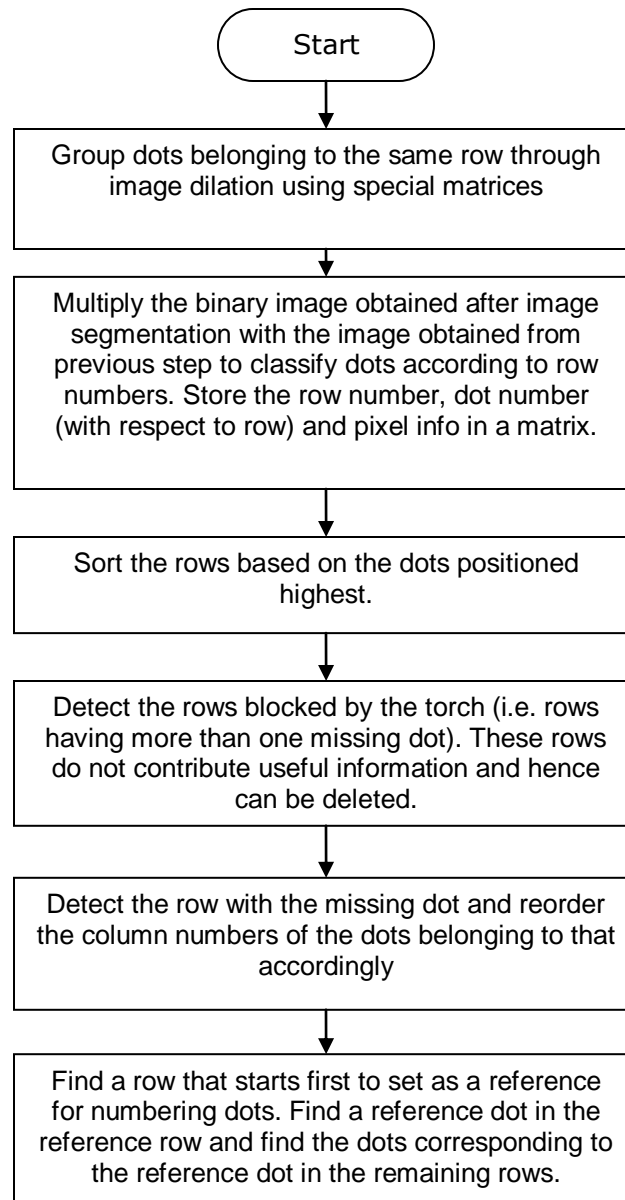


Figure 3-5 Flowchart of “feature extraction”

As can be observed in the flowchart, initially dilation is performed using specially designed structural elements to extract a row of dots at a time. The row numbers of the dots are found first and later column numbers are found.

Thus, by choosing a different welding direction that resulted in a denser reflected dot matrix pattern to improve the accuracy of surface reconstruction, better methods had to be proposed to face the new challenges posed. The same

algorithm could not be used for the new reflected images for the following reasons. In the previous method, the image is directly thresholded (refer Figure 2-11) and then noise removal is performed which is not the best way to segment an image. Preprocessing the image is necessary for better results. Also, extraction of the position for the new reflected images is more complicated due to the increased density of dots. The proposed method is better suited to the new reflected images. The next couple of chapters give detailed explanation of the techniques used to extract the features or the dots from the reflected images and calculate their positions.

CHAPTER 4

FEATURE EXTRACTION

The first step in feature extraction is to pre-process the image or estimate the unknown signal of interest from the available noisy data. As seen in Figure 4-1, the images are full of noise and of very low contrast. The reflected dots can be barely recognizable and have varying intensity, i.e. dots in the lower rows have greater intensity compared to dots in upper rows. If such an image is directly sent to image segmentation block, the result is cluttered with noise as can be seen in Figure 4-3. Thus, pre-processing the image is necessary to reduce the noise and improve the contrast making it ready for further processing.

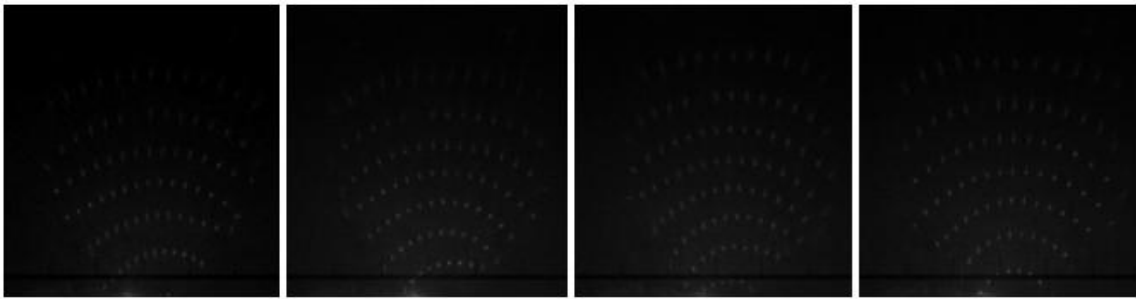


Figure 4-1 Acquired Reflected images using negative y-axis as welding direction

All the steps involved in pre-processing of the image can be illustrated in the form of a block diagram as shown in Figure 4-2.

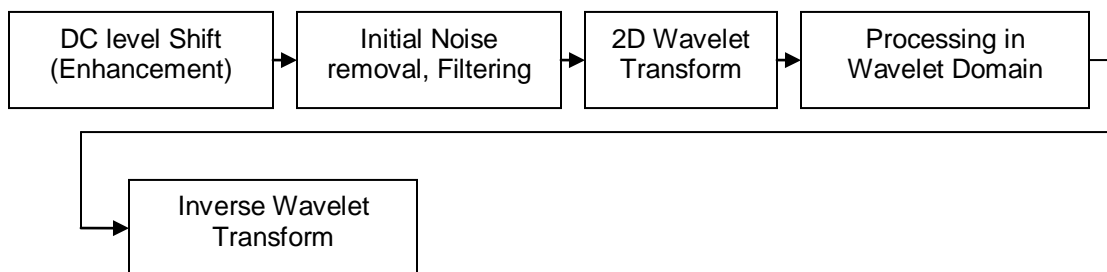


Figure 4-2 Preprocessing stage Block diagram

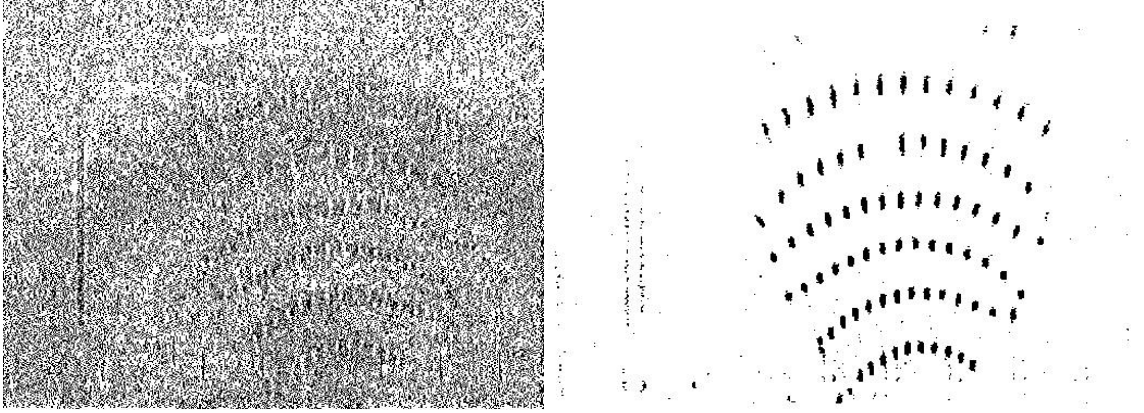


Figure 4-3 (a) Segmentation without preprocessing (b) with preprocessing

4.1 DC Level Shift

The first step in preprocessing is DC level shifting. Each pixel is subtracted from the highest pixel value in the whole image. The strong illumination gradient in the image makes it difficult to process the image. This is a very important step as segmentation with and without DC level shifting is illustrated in Figure 4-4.

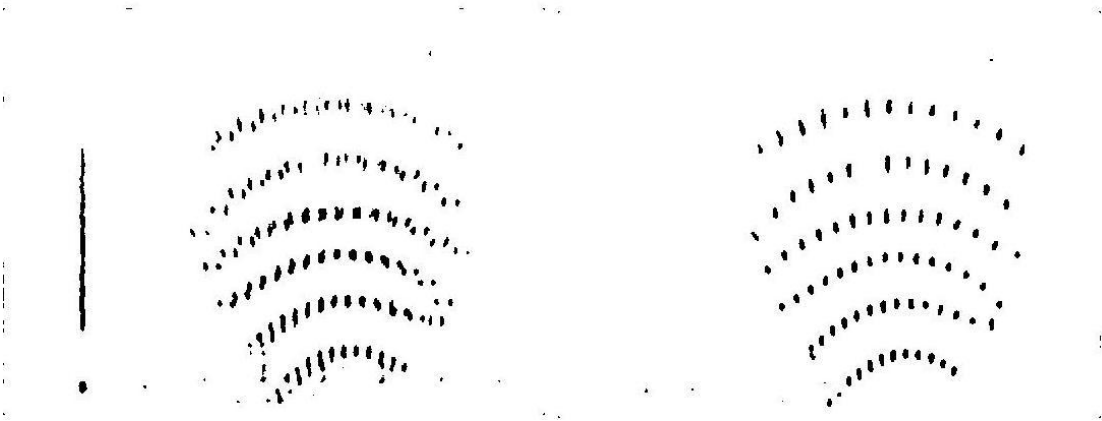


Figure 4-4 Segmentation without DC level shift and with DC level shift

4.2 Noise Removal using Wavelet Transform

The major factors affecting the amount of noise in the images acquired by the camera are the light levels and sensor temperature [28]. There are several ways

to reduce noise in an image. The method chosen for this particular application is the one based on wavelet transform.

Assume the observed data is $X(t) = S(t) + N(t)$, where $S(t)$ is the uncorrupted signal with additive noise $N(t)$. Let $W(.)$ and $W^{-1} (.)$ denote the forward and inverse transforms. Let $D(.,\lambda)$ denote the denoising operator with threshold λ . We intend to denoise $X(t)$ to recover $S^\wedge(t)$ as an estimate of $S(t)$. The procedure is summarized in three steps. [29]

$$Y = W(X)$$

$$Z = D(Y, \lambda)$$

$$S^\wedge = W^{-1}(Z)$$

“Wavelet transform” is emerging as the key transform of all other transform techniques. The inherent multi resolution analysis capability with the ability to give true time-frequency (scale) representation at variable resolutions makes wavelet transforms as the most versatile one. This overcomes the basic shortcoming of Fourier analysis, which is that the Fourier spectrum contains only globally averaged information, so leading to location specific features in the signal being lost. Applications of wavelet analysis are now widespread and cover many fields of scientific research including image analysis, medical science, astronomy, acoustics, nuclear engineering, magnetic resonance imaging, speech discrimination, optics, fractals, geophysics, engineering, fluid turbulence, financial analysis, earthquake-prediction, radar, human vision, and pure mathematics applications such as solving partial differential equations.

The wavelet analysis procedure is to adopt a wavelet prototype function, called an "analyzing wavelet" or "mother wavelet." Temporal analysis is performed with a contracted, high frequency version of the prototype wavelet, while frequency analysis is performed with a dilated, low frequency version of the prototype wavelet. Because the original signal or function can be represented in terms of a wavelet expansion (using coefficients in a linear combination of the wavelet functions), data operations can be performed using just the corresponding wavelet coefficients. The continuous wavelet transform of a signal (1D wavelet transform) is defined as follows

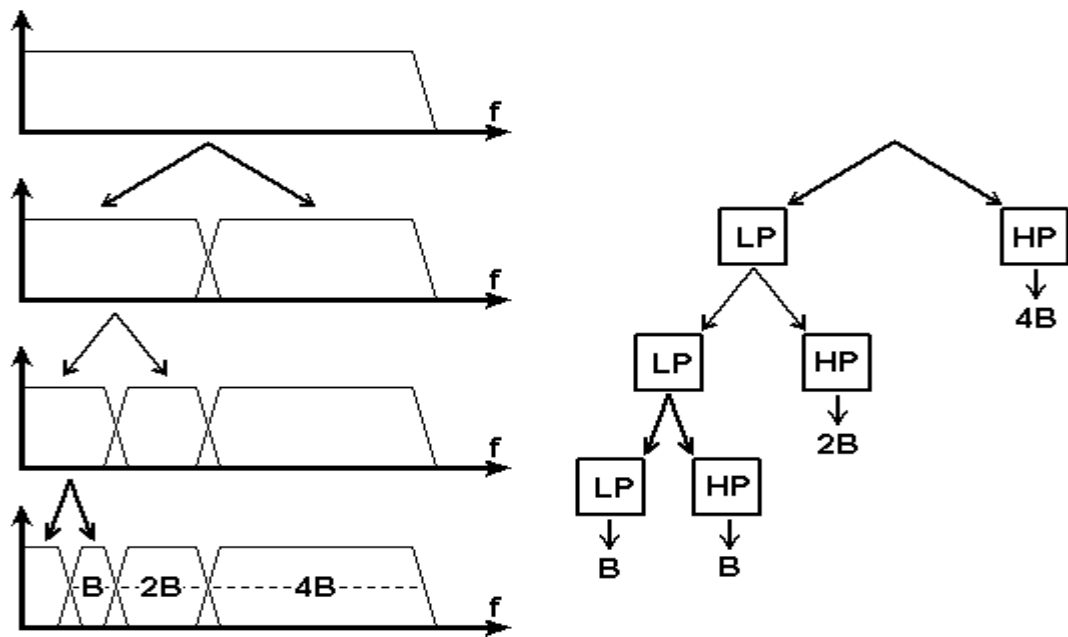
$$\gamma(s, \tau) = \int f(t) \varphi_{s,\tau}^*(t) dt$$

Wavelets are generated from a single basic wavelet $\psi(t)$, the *mother wavelet*, by scaling and translation:

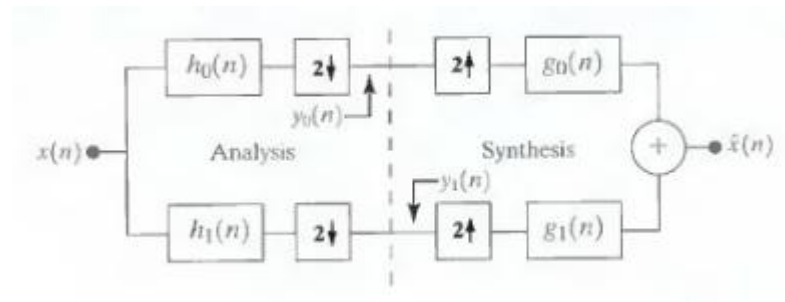
$$\varphi_{s,\tau}(t) = \frac{1}{\sqrt{s}} \varphi\left(\frac{t - \tau}{s}\right)$$

where s is the scale factor, τ is the translation factor and the factor $s^{-1/2}$ is for energy normalization across the different scales. Calculating wavelet coefficients at every possible scale is a fair amount of work, and it generates a lot of data. "Discrete wavelet transform" (DWT) can be obtained by choosing scales and positions based on powers of two. An efficient way to implement this is to use filters. Thus, if we regard the wavelet transform as a filter bank then we can consider wavelet transforming an image as passing the image through this filter bank. In subband coding, an image is decomposed into a set of band- limited

components, called subbands, which can be reassembled to reconstruct the original image without error. Each subband is generated by bandpass filtering the input. Since the bandwidth of the resulting subbands is smaller than that of the original image, the subbands can be downsampled without loss of information. Reconstruction of the original image is accomplished by upsampling, filtering, and summing the individual subbands.



(a) WT represented as a filter bank. (LP stands for lowpass filter and HP stands for high pass filter)



(b) Analysis and synthesis filter banks.

Figure 4-5 Subband coding

Since images are two-dimensional functions, two-dimensional DWT is to be considered for processing them. Like the one-dimensional DWT, the two-dimensional DWT can also be implemented using digital filters and down samplers. With separable two-dimensional scaling and wavelet functions, we simply take the one-dimensional Fast WT of the rows of $f(x, y)$, followed by the one-dimensional Fast WT of the resulting columns. Thus 2D DWT can be defined as follows.

$$W\varphi(j_0, m, n) = \frac{1}{\sqrt{MN}} \sum_{x=0}^{M-1} \sum_{y=0}^{N-1} f(x, y) \varphi_{j_0, m, n}(x, y)$$

$$W^i_{\psi}(j, m, n) = \frac{1}{\sqrt{MN}} \sum_{x=0}^{M-1} \sum_{y=0}^{N-1} f(x, y) \psi^i_{j, m, n}(x, y)$$

$$i=\{H,V,D\}$$

The index i identifies the direction of the wavelets namely, Horizontal (H), Vertical (V) and Diagonal (D). $W\varphi(j_0, m, n)$ coefficients define an approximation of $f(x, y)$ at scale j_0 . The $W^i_{\psi}(j, m, n)$ coefficients add horizontal, vertical and diagonal details for scales $j \geq j_0$.

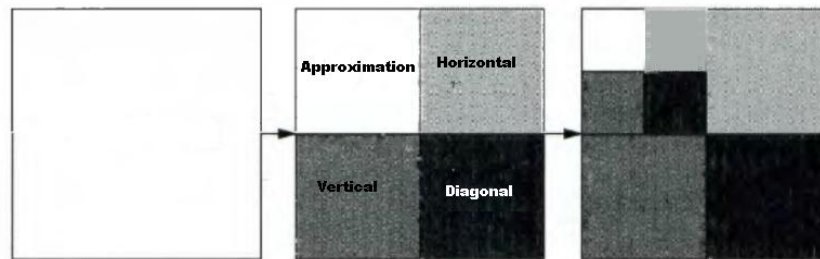


Figure 4-6 Result of 2D DWT of an image

The dots in the reflected dot matrix pattern are to be extracted from a background full of noise. A wavelet transformed reflected image is shown in Figure 4-7. It can be observed that the highest resolution image or the approximation image has both greater contrast and relatively less noise.

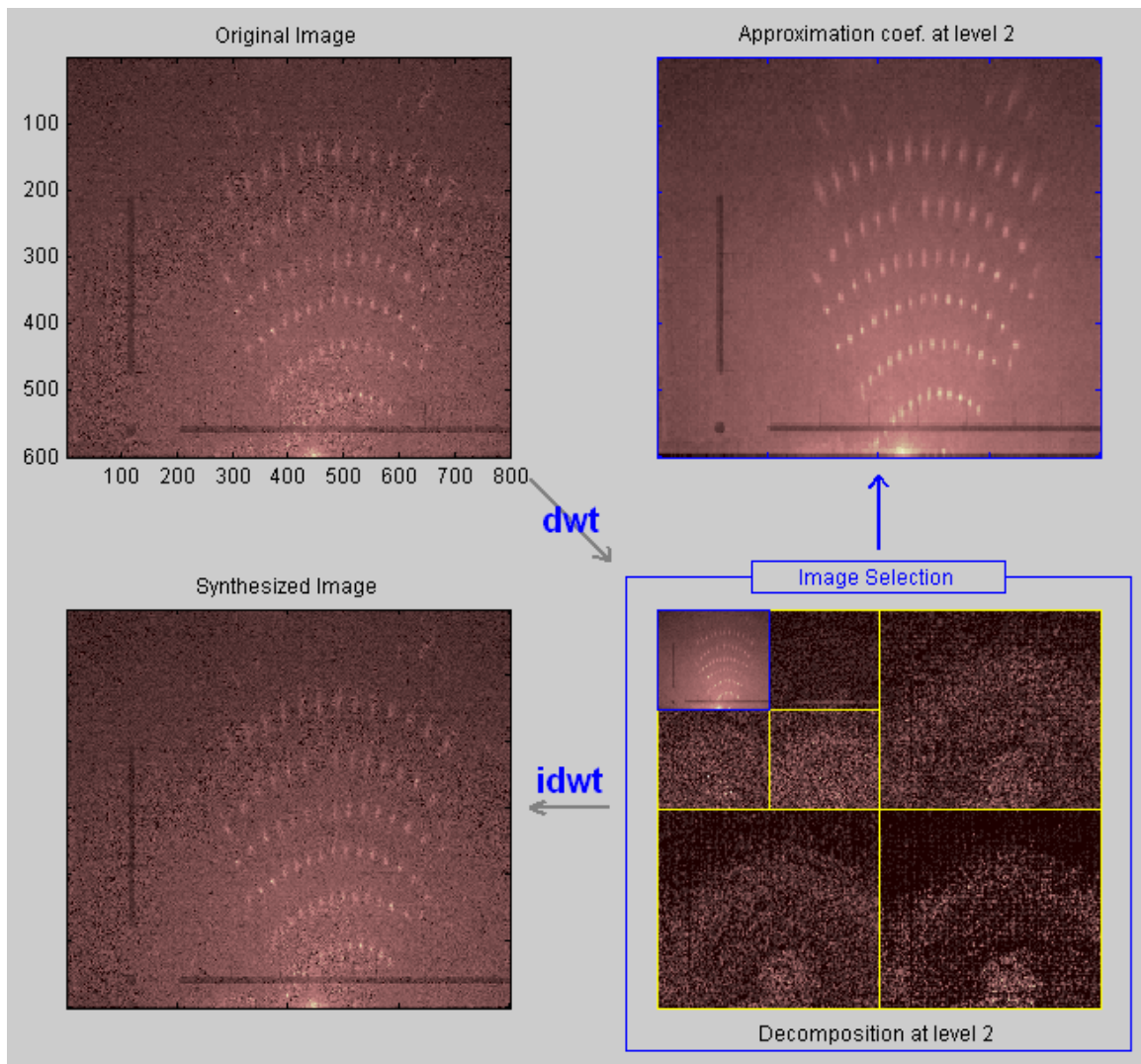


Figure 4-7 A sample reflected image is wavelet transformed using “sym6” wavelet at level two decomposition.

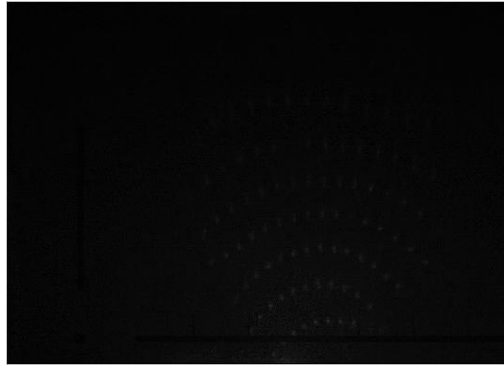
As can be observed, the highest resolution image after decomposition has lesser noise and greater contrast. Hence, after DC level shifting, the next step is to

remove most of the noise using wavelet transform based techniques and filters (Gaussian and motion). The image is first passed through a block where initial noise removal is performed. Here, based on the observation that the dots belonging to the lower rows are of a greater intensity compared to the dots belonging to the upper rows, the lower and the upper rows are treated differently. Noise in the lower half of the reflected image might be considered as dots in the upper half. This is due to decreasing intensity of the dots as we move farther. If the whole image is treated the same way then either noise might be picked up in the lower rows or actual dots might not be recognized by the algorithm. Hence, the noise in the “lower half” of the image is removed using the already available functions for image denoising using wavelet transform in MATLAB (thresholding the wavelet coefficients is the usual method of image denoising using wavelet transform). Next, the whole image is filtered using a motion filter. It can thus be observed that the lower half of the image is processed twice for noise removal. This image is not yet ready to be segmented and needs to be further processed for better segmentation results.

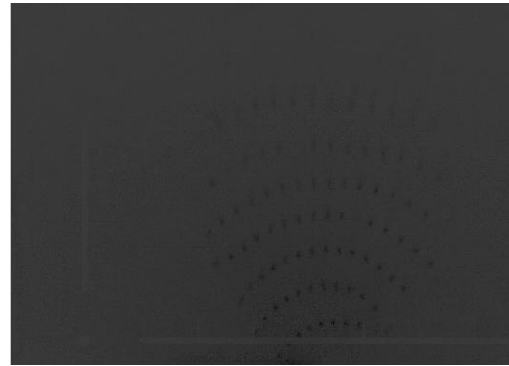
From the wavelet transform of this image, it can be observed that the detail coefficients have only noise. Thus, the technique here is to simply discard the detail coefficients and consider only the approximate coefficients. This is almost like thresholding the wavelet coefficients since not considering the detail coefficients is equivalent to equating them to zero.

Thus, the filtered image is 2D wavelet transformed at level 1 by using the “sym6” wavelet and then the approximate coefficient image is taken. Noise is further

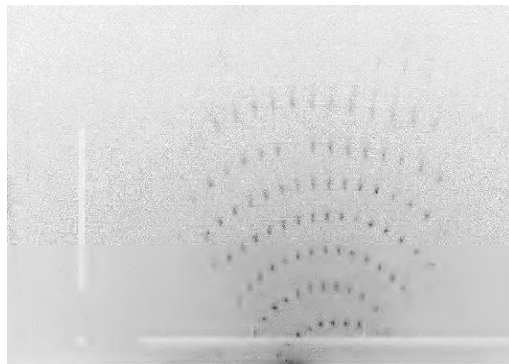
removed by filtering the approximate coefficient image using a Gaussian filter. The inverse wavelet transform of the Gaussian filtered image is then computed. The whole process is illustrated in Figures 4-8 and 4-9.



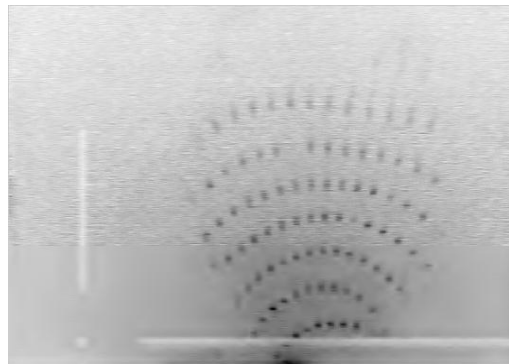
(a) Original Image



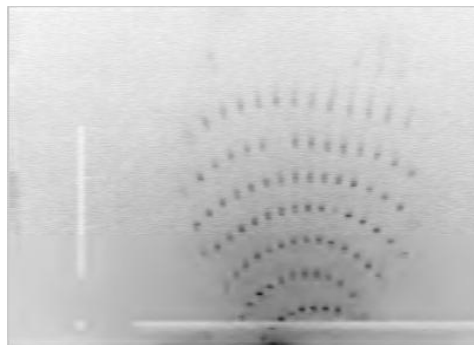
(b) After DC level shift



(c) After noise removal, treating lower half differently from the upper half

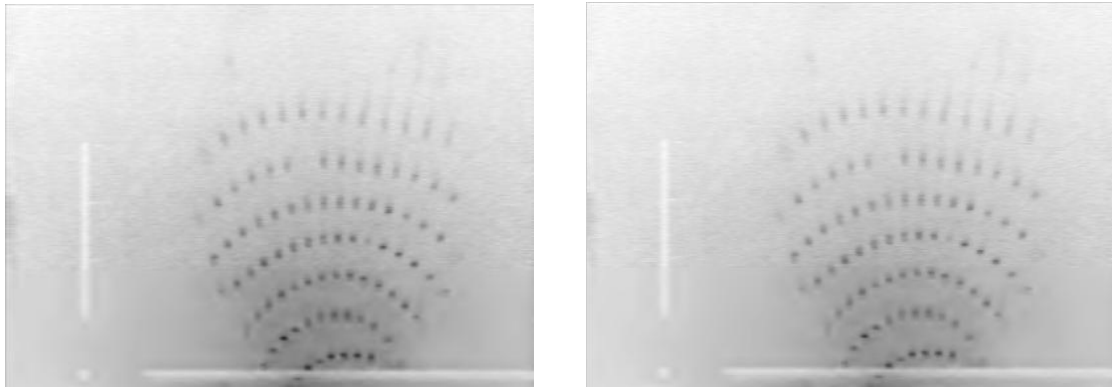


(d) After Filtering (using a motion filter)



(e) After Wavelet transform (actual image size of (d) is smaller than (c))

Figure 4-8 Various stages of Image preprocessing



(a) After Gaussian Filtering

(b) After inverse wavelet transform

Figure 4-9 Processing in Wavelet domain (actual image size of (a) is smaller than (b))

4.3 Image Segmentation

The preprocessed image has now relatively less noise and greater contrast. The next step is to extract the dots. This is done by segmenting the image. Segmentation subdivides an image into its constituent regions or objects. Image segmentation algorithms generally are based on one of two basic properties of intensity values: discontinuity and similarity. In the first category, the approach is to partition an image based on abrupt changes in intensity, such as edges in an image (edge detection). The principal approaches in the second category are based on partitioning an image into regions that are similar according to a set of predefined criteria. Thresholding, region growing, and region splitting and merging are examples of methods in this category. [29].

Both edge detection and thresholding were implemented and it was found that thresholding gives better results with less effort. The result of segmentation is a binary image.

4.3.1 Edge Detection

Edge detection is the process of locating edges in an image by detecting the prominent variations in intensity for a gray level image or in chrominance for a color image. Edge detecting an image significantly reduces the amount of data and filters out useless information, while preserving the important structural properties in an image [31]. Generally, an edge detection method can be divided into three stages.

In the first stage, a *noise reduction process* is performed. In order to gain better performance of edge detection, image noise should be reduced as much as possible. This noise reduction is usually achieved by using a low-pass filter because the additive noise is normally a high-frequency signal. However, the edges can possibly be removed at the same time because they are also high-frequency signals. Hence, a parameter is commonly used to make the best trade-off between noise reduction and edges information preservation.

In the second stage, a high-pass filter such as a differential operator is usually employed to *find the edges*.

In the last stage, an edge localization process is performed to identify the genuine edges, which are distinguished from those similar responses caused by noise. Thresholding techniques may be used to accomplish this process.

A variety of approaches for edge detection have been proposed for different purposes in different applications. Among the earliest works of edge detection are Sobel, Prewitt, Roberts, and Laplacian edge detectors, all of which use

convolution masks to approximate the first or second derivative of an image. In [30], an optimal filter for edge detection referred to *Canny edge detector*, was proposed. Three performance criteria defined for the optimality edge detection were “good detection, good localization, and unique answer to a true edge”. Canny edge detector has been used for segmentation of the reflected images. But the major problem with edge detection was that noise was getting falsely detected as dots and also it proved to be complicated to make the algorithm not to recognize the axis as a dot too.

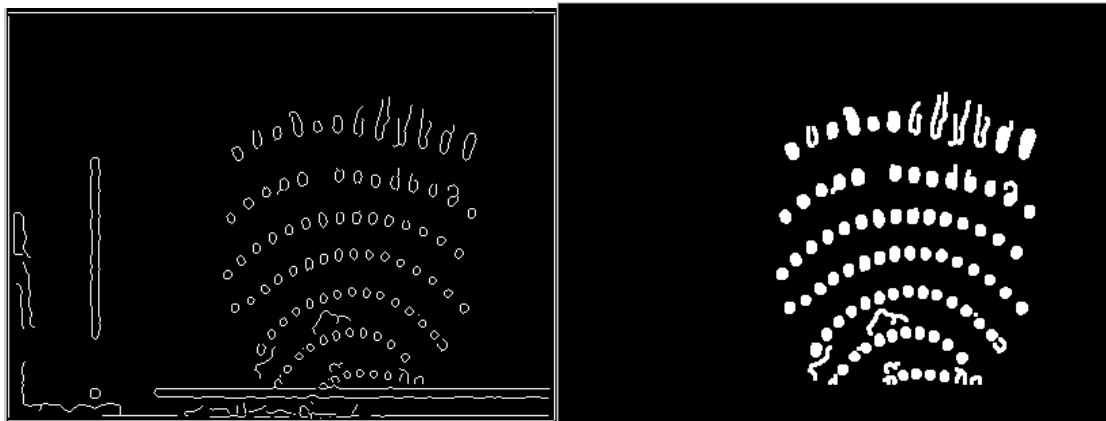


Figure 4-10 (a) After Canny edge detection (b) after removing noise and axis and filling the holes.

As shown in Figure 4-10, the axis's edges get recognized too. To remove such unwanted edges, an algorithm that calculates the perimeter of each connected dot needs to be found and if it does not fall within a range of normal dot size (to be assumed) then it would have to be removed. Apart from this, if the intensity of the dot is very less, the dot's edge might be broken. Although most of the noise is removed, the final segmented image is still not totally free of false edges. Using thresholding proved to be much simpler and effective.

4.3.2 Thresholding

Thresholding is a simple but effective tool to separate objects from the background. The output of thresholding is a binary image whose one state represents the foreground objects while the complementary state corresponds to the background. Simple thresholding would involve a single “global threshold” for the whole image and each pixel is compared to this threshold. All pixels having intensity below the threshold value are set to 0; the rest are set to 1. For global thresholding to work, the histogram of the input image should reveal two peaks, corresponding respectively to the signals from the background and the object. Global thresholding is as good as the degree of intensity separation between the two peaks in the image. It is an unsophisticated segmentation choice [32]. Hence this not a suitable choice of segmenting the dots in the reflected image since it has a strong illumination gradient.

The next option is “adaptive thresholding”. It divides the image into sub-images and thresholding is performed to that window. The assumption behind the method is that smaller image regions are more likely to have approximately uniform illumination, thus being more suitable for thresholding. This is useful for images with varying intensity like the reflected images under consideration. Local adaptive thresholding was found to be better compared to the computation intensive *Chow and Kanenko* approach. Image thresholded using the *Chow and Kanenko* approach is illustrated in Figure 4-11.

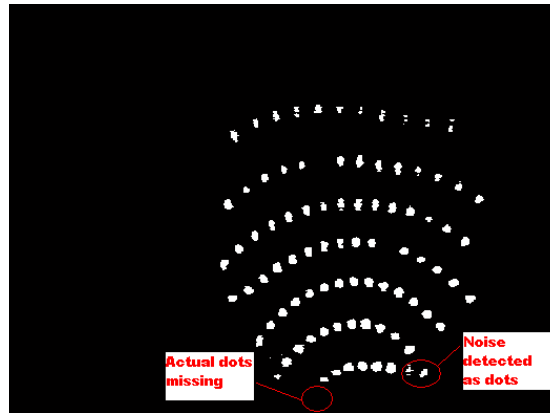


Figure 4-11 After Chow and Kanenko approach of adaptive thresholding

The usual method of finding the local threshold is to statistically examine the intensity values of the local neighborhood of each pixel. The best statistic depends largely on the input image. Simple and fast functions include the *mean* of the *local* intensity distribution, the median value or the mean of minimum and maximum values. The size of the neighborhood has to be large enough to cover sufficient foreground and background pixels, otherwise a poor threshold is chosen. On the other hand, choosing regions which are too large can violate the assumption of approximately uniform illumination. This method is less computationally intensive than the Chow and Kanenko approach and produces good results for our application.

The basic steps followed in thresholding the local adaptive way are given below.

1. Convolve the image with the statistical operator
2. Subtracting the original from the convolved image.
3. Thresholding the difference image with C (a constant)

Though the usual statistical operator is mean, it has been found that this does not work well with the reflected images as shown in Figure 4-12.

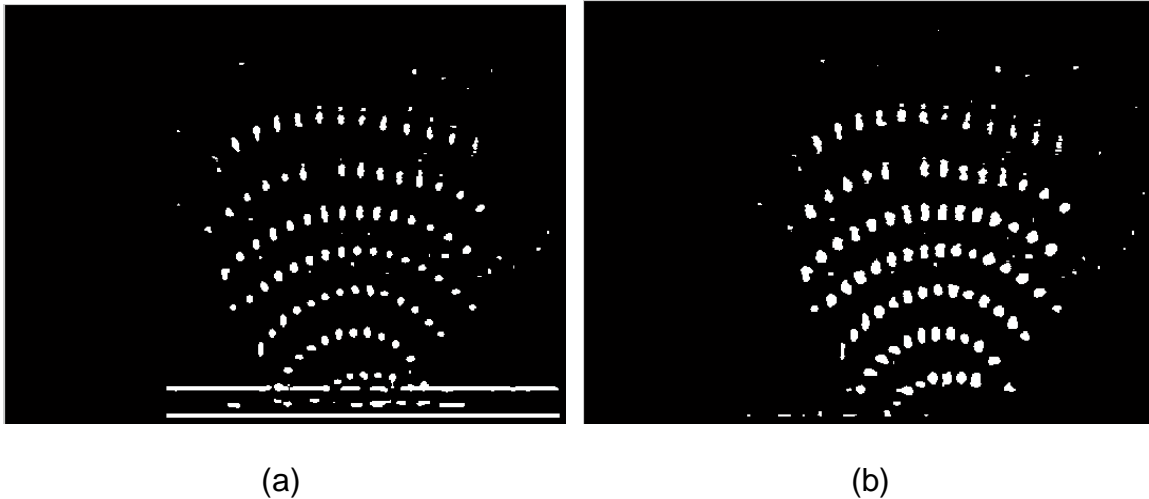


Figure 4-12. After thresholding using (a) mean (b) median as the statistical operator

For the reflected images, a 13x13 neighborhood has been chosen. The statistical operator that works best with these images is a special filter called “motion filter” (available in MATLAB). This filter, once convolved with an image, approximates the linear motion of a camera by 9 pixels, with an angle of 0 degrees in a counterclockwise direction. The filter becomes a vector for horizontal and vertical motions. Thus the input image is convolved with this motion filter and this convolved image is subtracted from the original image. Then, this difference image is thresholded with a constant “.01”. This is illustrated in Figure 4-13.

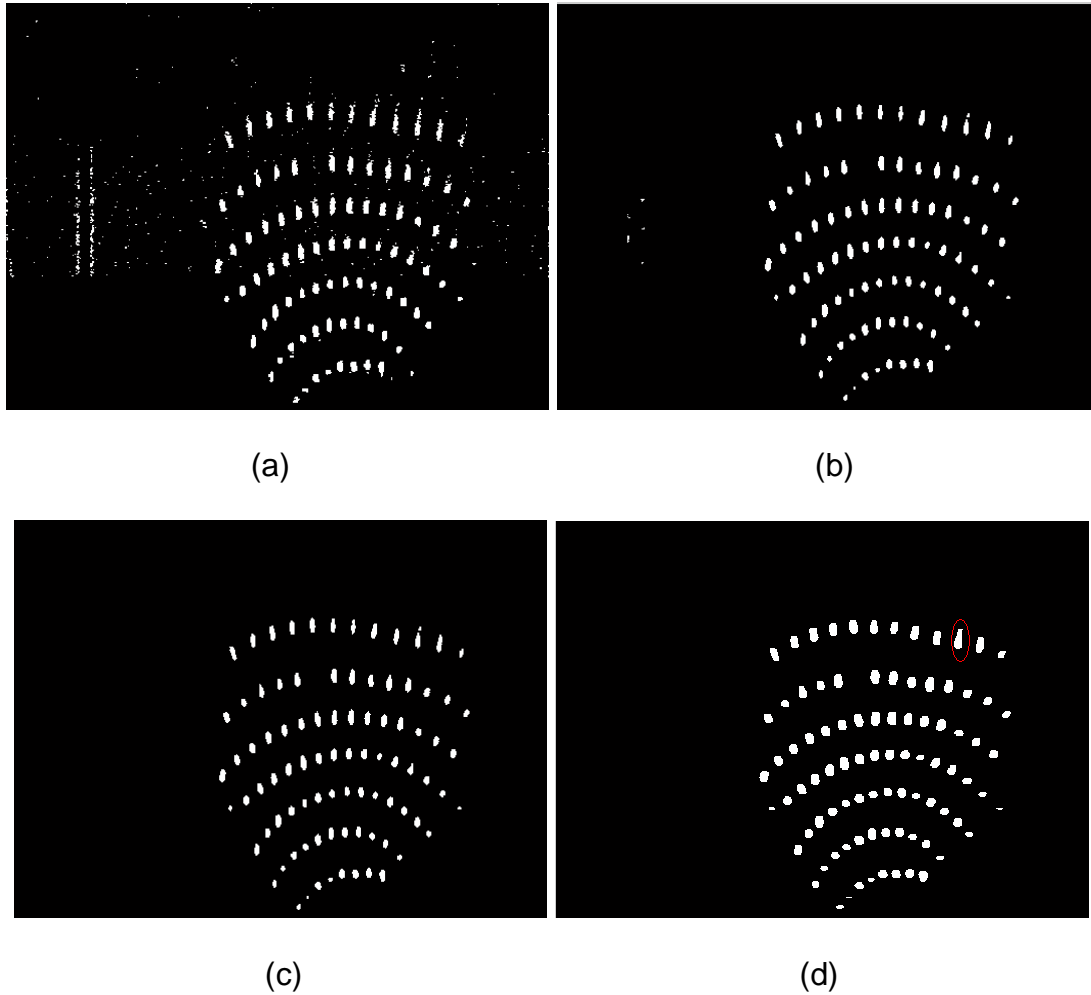


Figure 4-13 (a) After local adaptive thresholding using motion filter to convolve and a constant value of 0.01 (b) After median filtering (c) After removing vertical axis (d) After fixing broken dots by dilation and erosion

As can be observed in Figure 4-13 (a), the thresholded image has salt and pepper noise. The best way to remove salt and pepper noise is by median filtering. Median filtering is performed using a window consisting of an odd number of samples. The values in the window are sorted into numerical order; the median value, the sample in the center of the window, is selected as the output. The oldest sample is discarded, a new sample acquired, and the calculation repeats.

The result after median filtering is as shown in Figure 4-13 (b). There is still some noise due to the vertical axis line. Since the vertical axis position remains the same in every image and does not overlap with the reflected dot pattern (as the horizontal axis does), it can be removed. The resulting image is shown in Figure 4-13(c). A dot in the top most row is broken due to uneven intensity. This can be fixed by morphologically processing the image. Image dilation followed by erosion will result in a clean image as illustrated in Figure 4-13(d). The final step of segmentation is to shrink the dots to points so that a '1' in the binary image would mean the center position of a dot and a '0' would mean the background as shown in Figure 4-14.

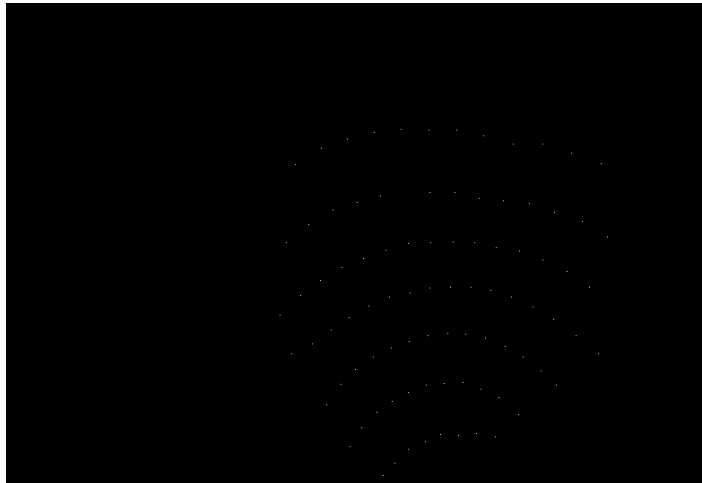


Figure 4-14. Binary Image where a dot is represented by a single pixel value of

'1'

POSITION ANALYSIS OF REFLECTED DOTS

This stage involves the extraction of row column information of the each dot in the reflected dot-matrix pattern. The entire algorithm is illustrated in a flowchart as follows. (Details involved in each step are given in the following sections).

5.1 Flowchart of the Algorithm

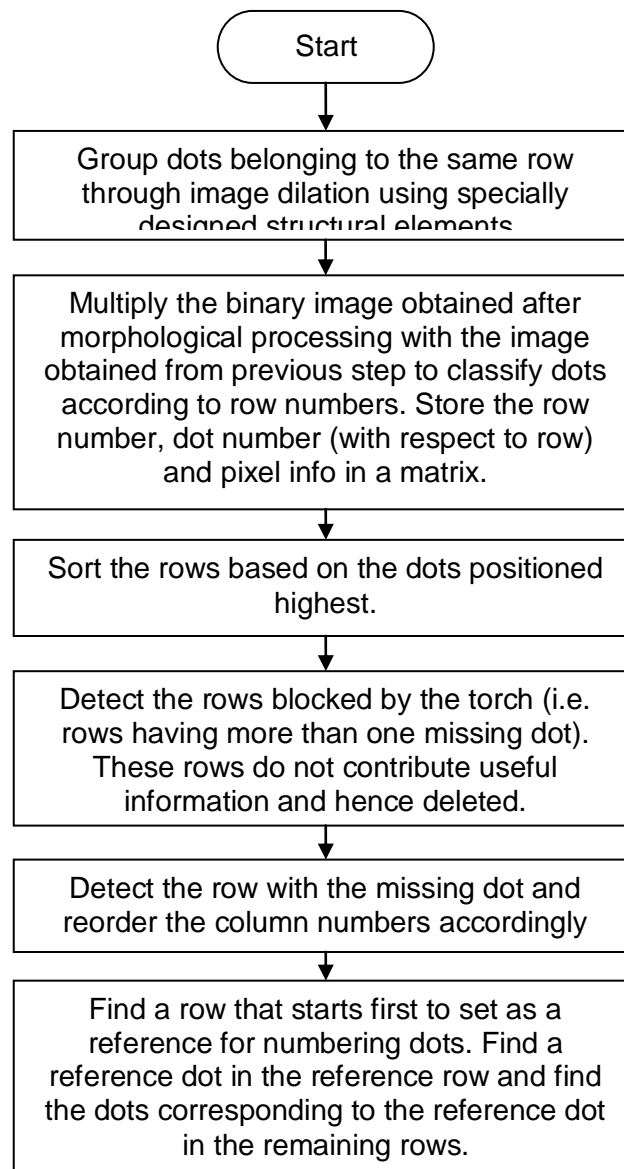


Figure 5-1. Flowchart of the Algorithm

5.2 Grouping of Dots According to Their Respective Rows

“It has been observed that in all reflected images, dots belonging to the same row are positioned closely together while dots belonging to different rows are farther apart”. This fact is used to group dots of same row.

The technique used here is image dilation. Image dilation, a fundamental operation in morphological processing may be defined as follows.

With A and B as sets in Z^2 , the dilation of A by B, denoted as $A \oplus B$, is defined as

$$A \oplus B = \{z | (\hat{B})_z \cap A \neq \emptyset\} \quad [28]$$

B is usually called structuring element and can also be viewed as a convolution mask. The basic effect of this operator on a binary image is to gradually enlarge the boundaries of regions of foreground pixels (*i.e.* white pixels, typically). Thus areas of foreground pixels grow in size while holes within those regions become smaller. The dilation operator takes two pieces of data as inputs. The first is the image which is to be dilated. The second is a (usually small) set of coordinate points known as a structuring element (also known as a *kernel*). It is this structuring element that determines the precise effect of the dilation on the input image. To compute the dilation of a binary input image by this structuring element, consider each of the *background* pixels in the input image in turn. For each background pixel (also called the *input pixel*) superimpose the structuring element on top of the input image so that the origin of the structuring element coincides with the input pixel position. If *at least one* pixel in the structuring element coincides with a foreground pixel in the image underneath, then the input pixel is set to the foreground value. If all the corresponding pixels in the

image are background however, the input pixel is left at the background value.
[33]

Now, the shape of the reflected dot matrix pattern is observed to be always convex. One way to group dots belonging to same rows is to dilate the dots to a predefined extent (determined based on the spacing between dots, same for all reflected images if dot-matrix pattern and welding direction remain unchanged) such that dots belonging to a particular row all join together to form one convex shaped curve. Now, each curve can be extracted from the binary image and when multiplied with the final binary image obtained after morphological processing will give a row of dots, i.e. dots belonging to a particular row are now known.

But, rows in the lower half of the reflected image have a greater curvature compared to that of rows in upper half. The spacing between such rows is also less. Thus, if the whole image is dilated in one particular way, the rows closely spaced to their neighboring rows may get connected. This is illustrated in the Figure 5.2.



Figure 5-2. Reflected image incorrectly dilated

Hence, each half of the image is dilated using a special structuring element. The structuring elements used in the algorithm are shown below in Figure 5-3 (a) and (b).

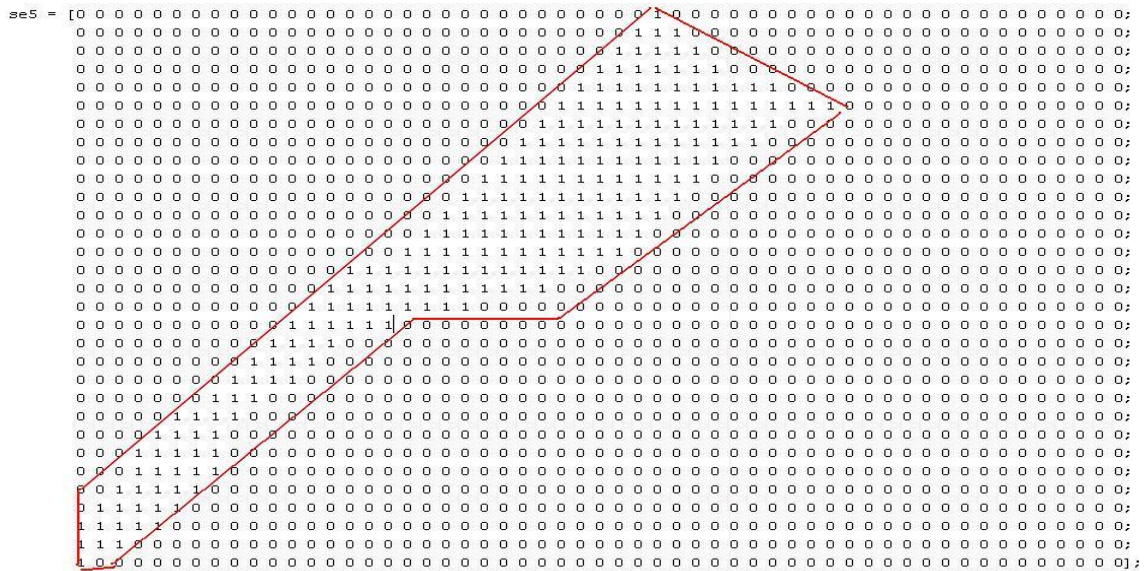


Figure 5-3 (a) Structuring element used to dilate the left half of the convex shaped dot pattern

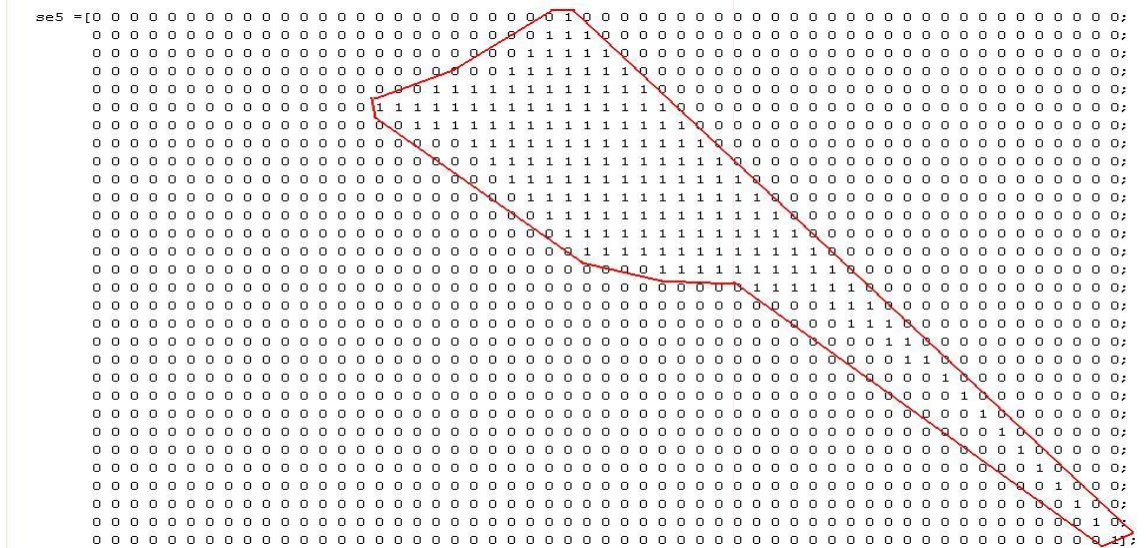
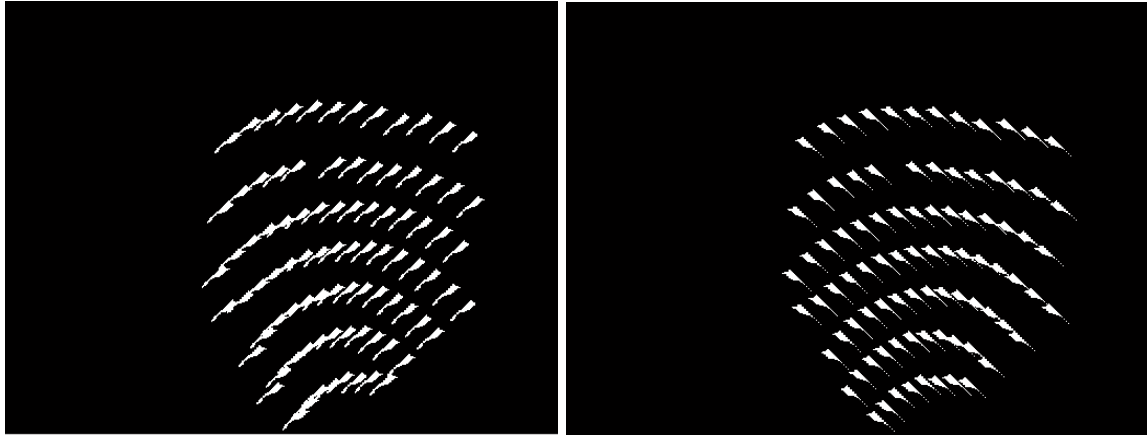


Figure 5-3 (b) Structuring element used to dilate the right half of the convex shaped dot pattern

Observe the shape of the '1's in the structuring elements in Figures 5-3 (a) and (b) (marked by the red line). The reason for choosing such a shape is the convex nature of the reflected dot matrix pattern. The long thin tail will take care of dots of same row but spaced farther apart. The short broad head will take care of closely spaced dots.

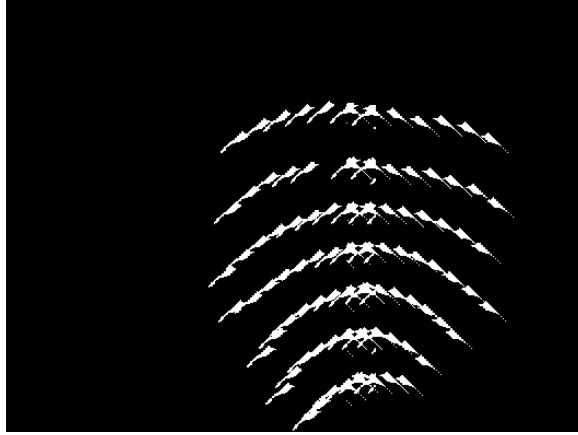


(a) Using structuring element 1

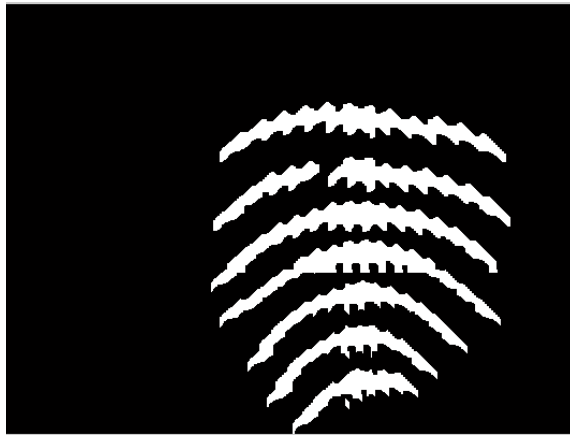
(b) Using structuring element 2

Figure 5-4 Final binary image dilated using special matrices

The whole image is dilated with structuring elements 1 and 2 separately as shown in Figure 5-4 (a) and (b). Then the width of the pattern is calculated and the midpoint is found. Using this midpoint, Figure 5-4 (a) and (b) are combined to get the image shown in Figure 5-5 (a). It can be observed that some dots in the upper rows and a few in the lower rows are not connected. At this stage, the whole image can be dilated using rectangular structuring elements Figure 5-5 (b).



(a) Combined image



(b) After dilation using rectangular structuring elements



(c) After further processing (opening)

Figure 5-5 Dilated Images

Figure 5-5 (b) has a few thin protrusions and breaks. The best way to get rid of these is morphologically opening the binary image. Opening generally smooths the contour of an object, breaks narrow isthmuses, and eliminates thin protrusions as observed in Figure 5-6. Opening of set A by structuring element B is defined as

$$A \circ B = (A \ominus B) \oplus B.$$

Thus, the opening A by B is the erosion of A by B , followed by a dilation of the result by B . The opening operation has a simple geometric interpretation (Figure 5-6). Suppose that we view the structuring element B as a (flat) "rolling ball." The boundary of $A \circ B$ is then established by the points in B that reach the farthest into the boundary of A as B is rolled around the inside of this boundary. This geometric fitting property of the opening operation leads to a set-theoretic formulation, which states that the opening of A by B is obtained by taking the union of all translates of B that fit into A .

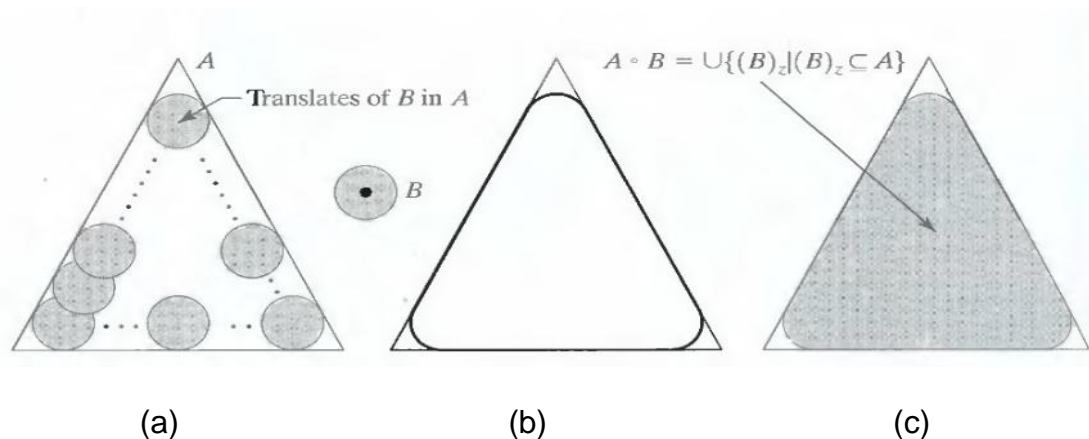


Figure 5-6 (a) Structuring element B "rolling" along the inner boundary of A (the dot indicates the origin of B). (b) The heavy line is the outer boundary of the opening, (c) Complete opening (shaded).

The morphologically opened image is shown in Figure 5-5 (c). In the binary image shown in Figure 5-5 (c), a '1' represents a row while a '0' represents the background. Note the discontinuity in the second row from the top in Figure 5-5 (b). This is due to the missing dot. This will mean that instead of considering that particular row as a single row, the algorithm will count two rows. This will be taken care of in the later stages.

5.3 Extracting the Dots of Each Row

Each row of the image in Figure 5-5 (c) is multiplied with the image shown in Figure 4-14 to obtain dots belonging to that particular row.

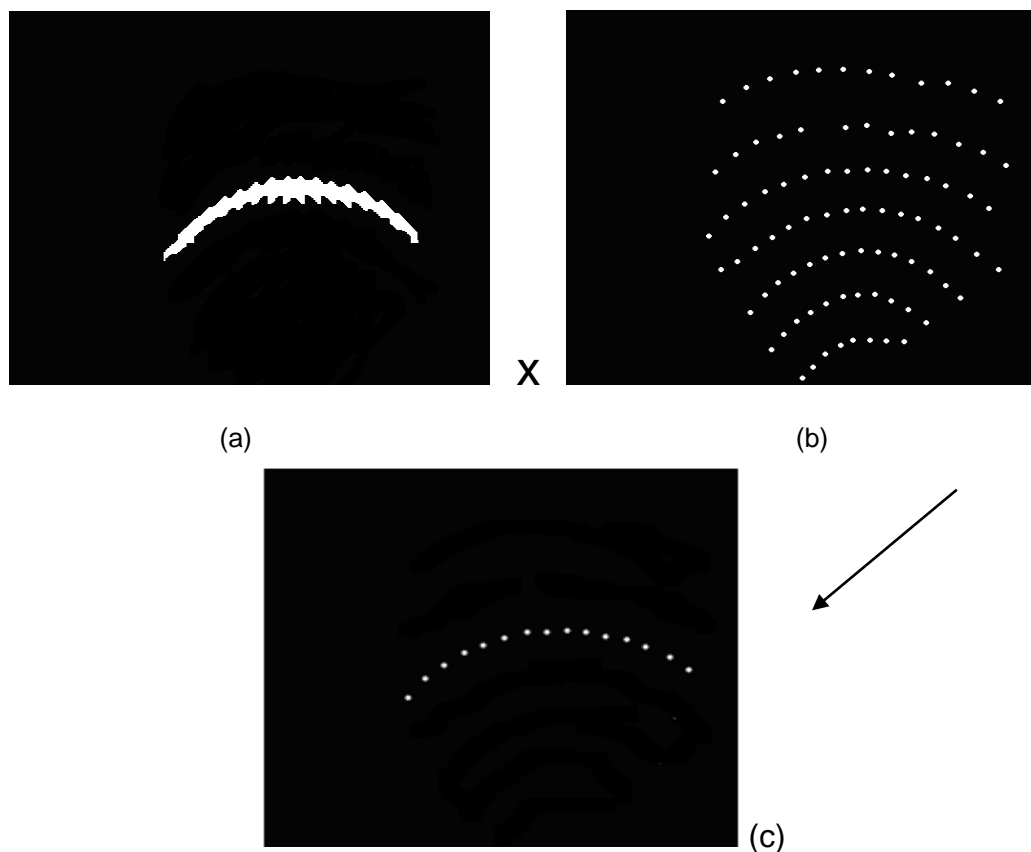


Figure 5-7. (a) Multiplied with (b) will result in (c). Dots in (b) and (c) are enlarged for better viewing in the document. In the actual case, a dot is represented by a single pixel value.

Table 5-1 Matrix storing the row, column and position information of each dot

Row	Col	Pixel info		Row	Col	Pixel info		Row	Col	Pixel info	
1	1	312	385	2	1	319	297	3	1	329	202
1	2	335	361	2	2	344	275	3	2	358	182
1	3	357	343	2	3	371	257	3	3	387	171
1	4	381	327	2	4	398	248	3	4	417	163
1	5	405	316	2	5	424	240	3	5	447	159
1	6	430	306					3	6	478	160
1	7	455	298					3	7	509	160
1	8	480	297					3	8	539	167
1	9	505	296					3	9	572	177
1	10	529	297					3	10	605	177
1	11	553	303					3	11	637	188
1	12	579	307					3	12	670	201
1	13	605	318								
1	14	632	332								
1	15	657	351								
4	1	325	432	5	1	364	494	6	1	390	545
4	2	348	420	5	2	380	469	6	2	403	522
4	3	369	403	5	3	396	451	6	3	420	503
4	4	389	388	5	4	416	436	6	4	437	490
4	5	411	374	5	5	436	425	6	5	455	479
4	6	434	363	5	6	456	417	6	6	475	470
4	7	457	358	5	7	477	410	6	7	495	468
4	8	479	352	5	8	499	407	6	8	516	467
4	9	502	351	5	9	519	408	6	9	536	475
4	10	525	351	5	10	541	413	6	10	556	485
4	11	547	355	5	11	563	423	6	11	578	506
4	12	570	363	5	12	583	436				
4	13	594	375	5	13	603	453				
4	14	617	390	5	14	620	470				
4	15	642	410								
4	16	667	432								
7	1	427	580	8	1	479	236				
7	2	440	565	8	2	507	236				
7	3	455	548	8	3	534	243				
7	4	474	539	8	4	561	246				
7	5	491	530	8	5	590	249				
7	6	511	531	8	6	618	260				
7	7	531	529	8	7	649	271				
7	8	552	533	8	8	677	290				

After obtaining image as shown in Figure 5-7 (c), the dots belonging to a particular row can be extracted by scanning the whole image for a pixel value of 1. Whenever we hit a pixel value of '1' (i.e. a dot has been extracted), the pixel information (or the position of the dot) is stored in a matrix along with the row number (the first row to be extracted is named 1 and the remaining are named in an increasing order, the actual order is taken care of in the later stages) and the column number (the first column to be extracted is named 1 and the succeeding dots of the same row are named in an increasing order). This can be repeated until all the dots of all the rows are extracted. The resulting matrix for a test image is tabulated and shown in Table 5-1. It can be observed from the Table 5-1 that the algorithm detected 8 rows (extra row due to the discontinuity in the row with a missing dot). The position of each dot (pixel info) in the image is also stored. But, though each dot now has a row number attached to it, the row number might not be correct. The row numbers need to be sorted such that they match with those shown in Figure 5-8. This sorting is done by first finding the highest positioned dot (i.e. dot with highest value in the z-coordinate of the universal coordinate system) in each row and then sorting the rows based on that.

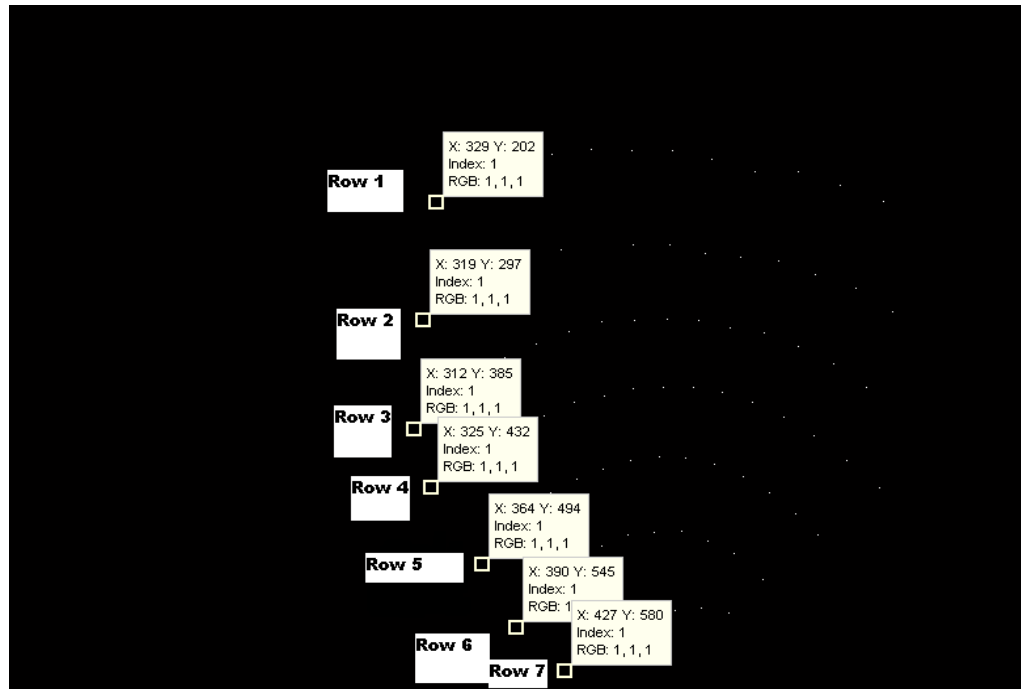


Figure 5-8. The first dot of each row is marked with its pixel info and row number
After finding the highest positioned points of each row, a matrix with their row numbers, column numbers and their pixel info is created as shown below.

Table 5-2 Matrix storing the highest positioned dot in each row

Row	Col	Pixel_info_x	Pixel_info_x
1	9	505	296
2	5	424	240
3	5	447	159
4	9	502	351
5	8	499	407
6	8	516	467
7	7	531	529
8	1	479	236

These dots are marked with their pixel info and shown in Figure 5-9.

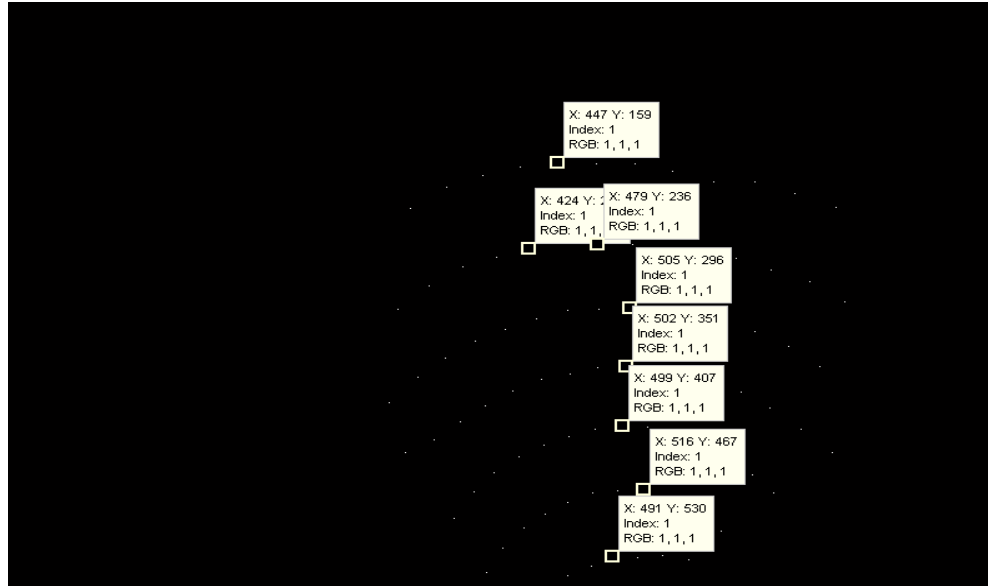


Figure 5-9. The highest positioned point of each row is marked.

Now the matrix is sorted in ascending order on column 3. This would result in

Table 5-3 Matrix with rows sorted according to the highest positioned dots

Row	Col	Pixel_info_x	Pixel_info_y
3	5	447	159
8	1	479	236
2	5	424	240
1	9	505	296
4	9	502	351
5	8	499	407
6	8	516	467
7	7	531	529

The values in the table 5-3 indicate that row 3 should actually be row 1, row 8 should be row 2, row 2 should be row 3 and so on. Now the matrix which stores the information of all dots is updated with the new row numbers as shown below.

Table 5-4 Matrix with the updated row numbers

Row	Col	Pixel info		Row	Col	Pixel info		Row	Col	Pixel info	
4	1	312	385	3	1	319	297	1	1	329	202
4	2	335	361	3	2	344	275	1	2	358	182
4	3	357	343	3	3	371	257	1	3	387	171
4	4	381	327	3	4	398	248	1	4	417	163
4	5	405	316	3	5	424	240	1	5	447	159
4	6	430	306					1	6	478	160
4	7	455	298					1	7	509	160
4	8	480	297					1	8	539	167
4	9	505	296					1	9	572	177
4	10	529	297					1	10	605	177
4	11	553	303					1	11	637	188
4	12	579	307					1	12	670	201
4	13	605	318								
4	14	632	332								
4	15	657	351								
5	1	325	432	6	1	364	494	7	1	390	545
5	2	348	420	6	2	380	469	7	2	403	522
5	3	369	403	6	3	396	451	7	3	420	503
5	4	389	388	6	4	416	436	7	4	437	490
5	5	411	374	6	5	436	425	7	5	455	479
5	6	434	363	6	6	456	417	7	6	475	470
5	7	457	358	6	7	477	410	7	7	495	468
5	8	479	352	6	8	499	407	7	8	516	467
5	9	502	351	6	9	519	408	7	9	536	475
5	10	525	351	6	10	541	413	7	10	556	485
5	11	547	355	6	11	563	423	7	11	578	506
5	12	570	363	6	12	583	436				
5	13	594	375	6	13	603	453				
5	14	617	390	6	14	620	470				
5	15	642	410								
5	16	667	432								
8	1	427	580	2	1	479	236				
8	2	440	565	2	2	507	236				
8	3	455	548	2	3	534	243				
8	4	474	539	2	4	561	246				
8	5	491	530	2	5	590	249				
8	6	511	531	2	6	618	260				
8	7	531	529	2	7	649	271				
8	8	552	533	2	8	677	290				

Next, the pixel information of first dot, last dot, distance between first two dots, total number of dots, maximum positioned dot of each row are stored.

first_last = [row_num first_x last_y dist_btn_dots tot_number_of_dots max_dot_y]

Table 5-5 Matrix storing the information of first and last dot of each row, average distance between dots, total number of dots and highest positioned dot

Row	First_dot_x	Last_dot_x	Dist_btn_dots	Tot_dots	Max_dot_y
1	329	670	29	12	159
2	479	677	28	8	236
3	319	424	25	5	240
4	312	657	23	15	296
5	325	667	23	16	351
6	364	620	16	14	407
7	390	578	13	11	467
8	427	552	13	8	529

5.4 Identification and Deletion of Rows Blocked by the Torch

Rows blocked by the torch can be identified as rows with more than one missing dot. After dilation of rows, if the rows have one or more missing dots, they may not be connected. The row_col_info matrix might show them as two different rows. Hence, each row must be compared to the row before and row after it. If the difference between first dot of present row and last dot of next row OR difference between last dot of present row and first dot of next row is greater than twice the distance between dots of the same row AND the total number of dots in both the rows (individually and summation) is less than maximum number of dots

in the image, then, delete that row. The example being discussed does not have any rows with more than one missing dots. Hence, no row is deleted.

5.5 Detect the Row with One Missing Dot

For this, each row is scanned and if the distance between last dot of next row and first dot of present row OR distance between first dot of next row and last dot of present row is less than twice the distance between dots of present row then they actually belong to same row i.e discontinuity due to missing dots.

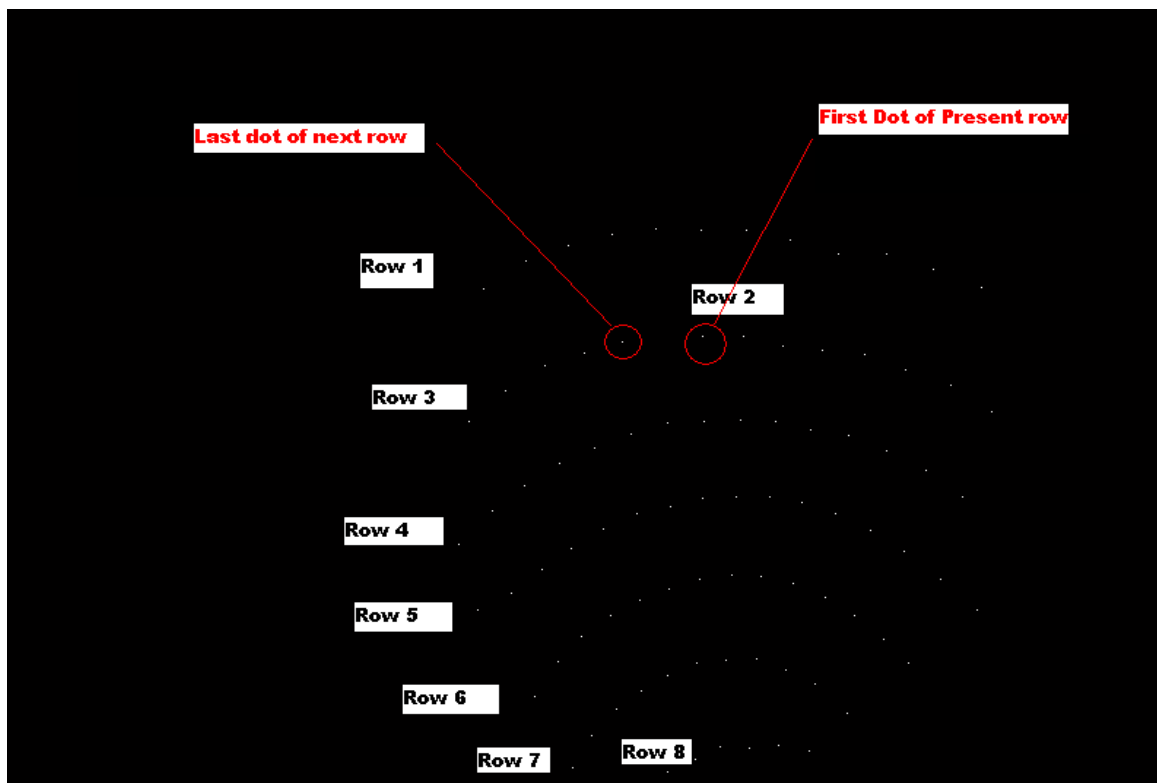


Figure 5-10 Image showing the row with the missing dot

In the example being discussed, rows 2 and 3 are actually one single row. After combining them, the following matrix is obtained.

Table 5-6 Matrix with discontinuities in the rows fixed

Row	Col	Pixel info		Row	Col	Pixel info		Row	Col	Pixel info	
3	1	312	385	2	1	319	297	1	1	329	202
3	2	335	361	2	2	344	275	1	2	358	182
3	3	357	343	2	3	371	257	1	3	387	171
3	4	381	327	2	4	398	248	1	4	417	163
3	5	405	316	2	5	424	240	1	5	447	159
3	6	430	306					1	6	478	160
3	7	455	298					1	7	509	160
3	8	480	297					1	8	539	167
3	9	505	296					1	9	572	177
3	10	529	297					1	10	605	177
3	11	553	303					1	11	637	188
3	12	579	307					1	12	670	201
3	13	605	318								
3	14	632	332								
3	15	657	351								
4	1	325	432	5	1	364	494	6	1	390	545
4	2	348	420	5	2	380	469	6	2	403	522
4	3	369	403	5	3	396	451	6	3	420	503
4	4	389	388	5	4	416	436	6	4	437	490
4	5	411	374	5	5	436	425	6	5	455	479
4	6	434	363	5	6	456	417	6	6	475	470
4	7	457	358	5	7	477	410	6	7	495	468
4	8	479	352	5	8	499	407	6	8	516	467
4	9	502	351	5	9	519	408	6	9	536	475
4	10	525	351	5	10	541	413	6	10	556	485
4	11	547	355	5	11	563	423	6	11	578	506
4	12	570	363	5	12	583	436				
4	13	594	375	5	13	603	453				
4	14	617	390	5	14	620	470				
4	15	642	410								
4	16	667	432								
7	1	427	580	2	1	479	236				
7	2	440	565	2	2	507	236				
7	3	455	548	2	3	534	243				
7	4	474	539	2	4	561	246				
7	5	491	530	2	5	590	249				
7	6	511	531	2	6	618	260				
7	7	531	529	2	7	649	271				
7	8	552	533	2	8	677	290				

In table 5-6, note that dots with row number 3 were updated with row number 2 and since two rows are now combined into one and so there is one less row, the remaining rows were updated too. Now, the total number of rows is 7. These values comply with those shown in Figure 5-8.

But, if the missing dot is in a row where the distance between consecutive dots in that row is small (like in the rows in the lower half of the reflected image), then there might be no discontinuity after image dilation. So, the previous step would not have been able to detect the missing dot. Hence, we scan all the rows again and check if the distance between consecutive dots of the same row is greater than twice the average distance between the dots. After the detection of missing dot, the dot numbers are re-ordered.

The next step is to find the position of the missing dot and updating the column numbers of the row to which it belongs. The column number of the dot preceding the missing dot is stored which will be useful later on. After updating this information, the final matrix will have the following values.

Table 5-7 Matrix with correct row numbers and updated missing dot position

Row	Col	Pixel info		Row	Col	Pixel info		Row	Col	Pixel info	
1	1	329	202	2	1	319	297	3	1	312	385
1	2	358	182	2	2	344	275	3	2	335	361
1	3	387	171	2	3	371	257	3	3	357	343
1	4	417	163	2	4	398	248	3	4	381	327
1	5	447	159	2	5	424	240	3	5	405	316
1	6	478	160	2	7	479	236	3	6	430	306
1	7	509	160	2	8	507	236	3	7	455	298
1	8	539	167	2	9	534	243	3	8	480	297
1	9	572	177	2	10	561	246	3	9	505	296
1	10	605	177	2	11	590	249	3	10	529	297
1	11	637	188	2	12	618	260	3	11	553	303
1	12	670	201	2	13	649	271	3	12	579	307
				2	14	677	290	3	13	605	318
								3	14	632	332
								3	15	657	351
4	1	325	432	5	1	364	494	6	1	390	545
4	2	348	420	5	2	380	469	6	2	403	522
4	3	369	403	5	3	396	451	6	3	420	503
4	4	389	388	5	4	416	436	6	4	437	490
4	5	411	374	5	5	436	425	6	5	455	479
4	6	434	363	5	6	456	417	6	6	475	470
4	7	457	358	5	7	477	410	6	7	495	468
4	8	479	352	5	8	499	407	6	8	516	467
4	9	502	351	5	9	519	408	6	9	536	475
4	10	525	351	5	10	541	413	6	10	556	485
4	11	547	355	5	11	563	423	6	11	578	506
4	12	570	363	5	12	583	436				
4	13	594	375	5	13	603	453				
4	14	617	390	5	14	620	470				
4	15	642	410								
4	16	667	432								
7	1	427	580								
7	2	440	565								
7	3	455	548								
7	4	474	539								
7	5	491	530								
7	6	511	531								
7	7	531	529								
7	8	552	533								

The red circle in Table 5-7 shows the position of the missing dot. It can be seen that 6th dot of the 2nd row is missing.

5.6 Updating the column numbers

The matrix `row_col_info_final` now has dots with correct row numbers but incorrect column numbers. They are local to their particular rows. They should be updated so that they are valid over the entire image. Refer Figures 5-11, 5-12.

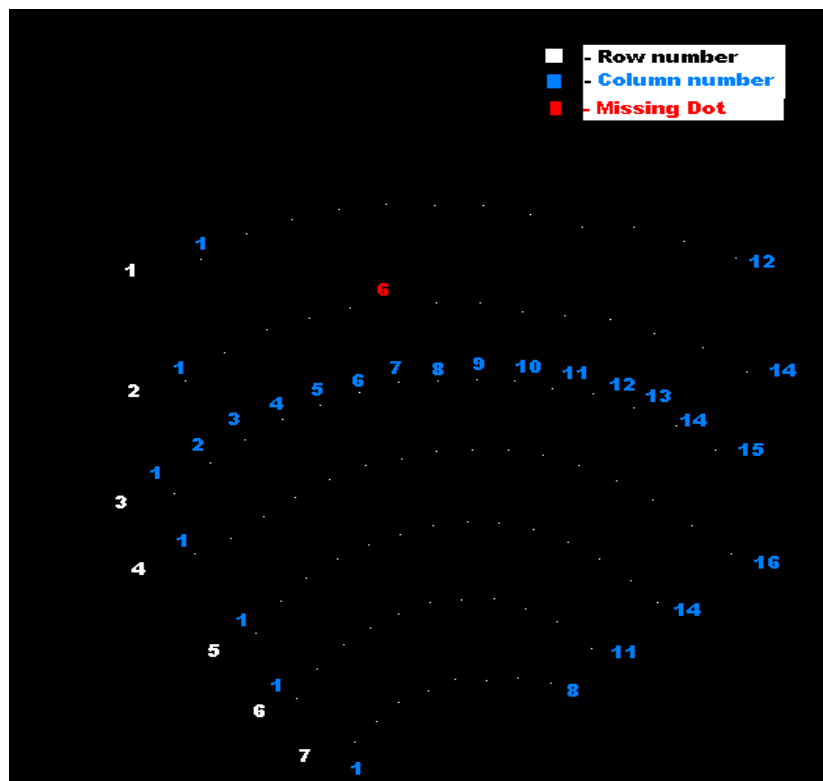


Figure 5-11 A color coded Binary image with the correct row numbers but localized column numbers.

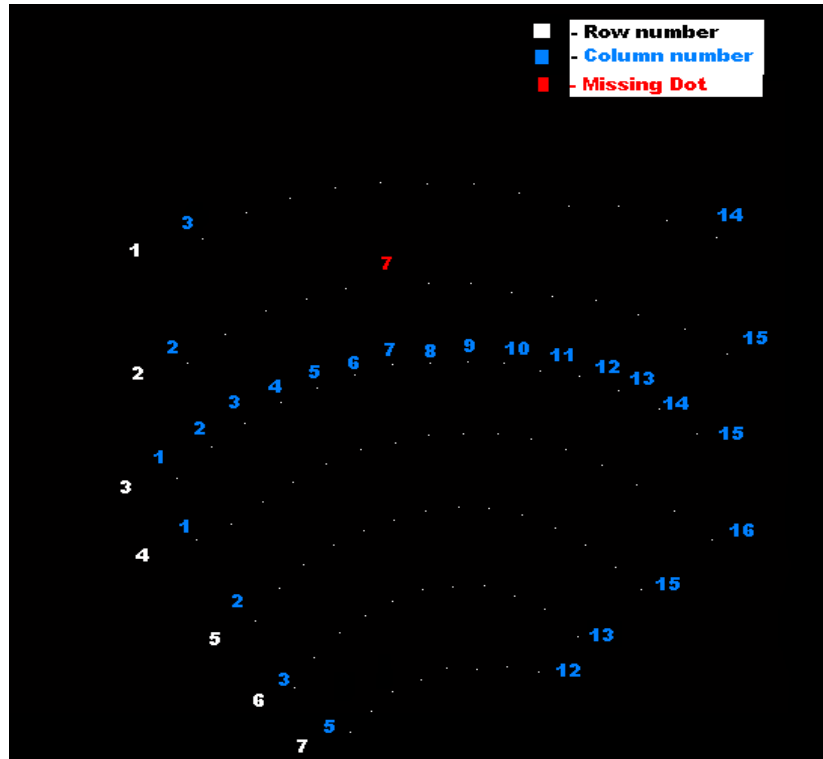


Figure 5-12 A color coded Binary image with the correct row and column numbers and missing dot number.

The row that starts first (the row 3 in the cited example) is taken as the reference row. The first dot in this row has the column number 1. Then, a dot that is approximately half way through the image is marked as the reference dot. This will be used to update the column numbers of other rows. It can be observed from Figure 5-13 that though the pattern is of convex shape, the dots corresponding to the reference dot fall on an approximately straight line passing through the reference dot.

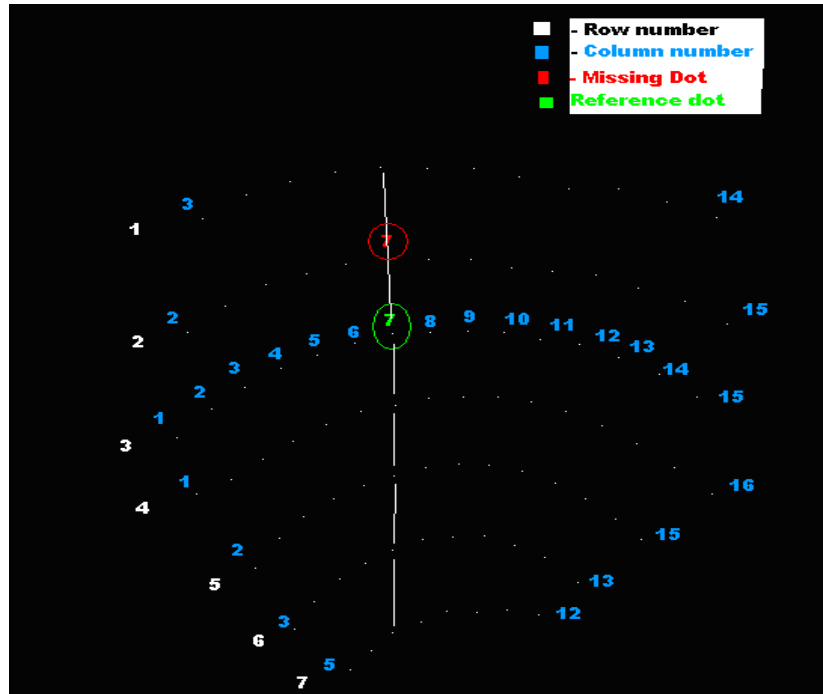


Figure 5-13 Binary image showing the reference dot and the line connecting the corresponding dots in the remaining rows.

The pixel info (x-axis value) of the reference column is stored. Now, each row other than the reference row is taken and each dot's x-axis value is compared with that of the reference dot. The dot with the x-axis value closest to that of reference dot is considered as the dot corresponding to the reference dot. This dot's column number is changed to a high number like 50. Thus when we scan through the row_col_info_final matrix, a value of 50 in a row will imply that it is a dot corresponding to the reference dot.

Table 5-8 Finding the dots corresponding to the reference dot (ref. row is 3, col. is 7)

Row	Col	Pixel info		Row	Col	Pixel info		Row	Col	Pixel info	
1	1	329	202	2	1	319	297	3	1	312	385
1	2	358	182	2	2	344	275	3	2	335	361
1	3	387	171	2	3	371	257	3	3	357	343
1	4	417	163	2	4	398	248	3	4	381	327
1	50	447	159	2	5	424	240	3	5	405	316
1	6	478	160	2	50	479	236	3	6	430	306
1	7	509	160	2	8	507	236	3	7	455	298
1	8	539	167	2	9	534	243	3	8	480	297
1	9	572	177	2	10	561	246	3	9	505	296
1	10	605	177	2	11	590	249	3	10	529	297
1	11	637	188	2	12	618	260	3	11	553	303
1	12	670	201	2	13	649	271	3	12	579	307
				2	14	677	290	3	13	605	318
								3	14	632	332
								3	15	657	351
4	1	325	432	5	1	364	494	6	1	390	545
4	2	348	420	5	2	380	469	6	2	403	522
4	3	369	403	5	3	396	451	6	3	420	503
4	4	389	388	5	4	416	436	6	4	437	490
4	5	411	374	5	5	436	425	6	50	455	479
4	6	434	363	5	50	456	417	6	6	475	470
4	50	457	358	5	7	477	410	6	7	495	468
4	8	479	352	5	8	499	407	6	8	516	467
4	9	502	351	5	9	519	408	6	9	536	475
4	10	525	351	5	10	541	413	6	10	556	485
4	11	547	355	5	11	563	423	6	11	578	506
4	12	570	363	5	12	583	436				
4	13	594	375	5	13	603	453				
4	14	617	390	5	14	620	470				
4	15	642	410								
4	16	667	432								
7	1	427	580								
7	2	440	565								
7	50	455	548								
7	4	474	539								
7	5	491	530								
7	6	511	531								
7	7	531	529								
7	8	552	533								

The matrix is next scanned through and where ever a 50 appears, it is replaced with the reference column number and the remaining column numbers of the same row are updated accordingly.

There is a special case when the missing dot corresponds to the reference column. In this case, either the dot preceding the missing dot or succeeding would be marked as the dot corresponding to the reference dot which is incorrect. To rectify this problem, a flag is raised (while marking the dots corresponding to reference dot with 50) if the column number of the dot being marked 50 not equal to the result of adding one to column number of the previous dot or to the result of subtracting one from column number of the next dot. After updating all the column numbers, we check for a raised flag. If it is, then the difference between the reference column number and the column number of the dot preceding the missing dot is computed. This difference minus one is then added to all the column numbers of the row with the missing dot. The final result is shown below. This information complies with the ones shown in Figure 5-11.

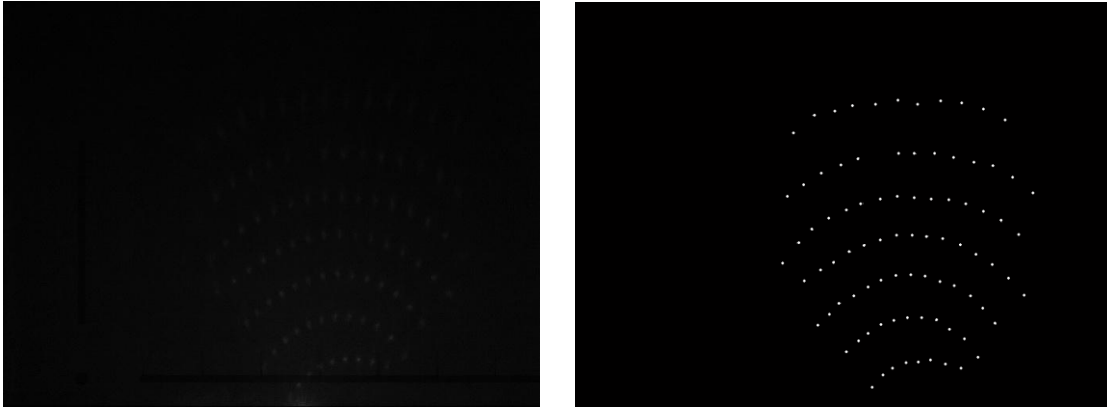
Table 5-9 Final matrix with correct row and column numbers

Row	Col	Pixel info		Row	Col	Pixel info		Row	Col	Pixel info	
1	3	329	202	2	2	319	297	3	1	312	385
1	4	358	182	2	3	344	275	3	2	335	361
1	5	387	171	2	4	371	257	3	3	357	343
1	6	417	163	2	5	398	248	3	4	381	327
1	7	447	159	2	6	424	240	3	5	405	316
1	8	478	160	2	8	479	236	3	6	430	306
1	9	509	160	2	9	507	236	3	7	455	298
1	10	539	167	2	10	534	243	3	8	480	297
1	11	572	177	2	11	561	246	3	9	505	296
1	12	605	177	2	12	590	249	3	10	529	297
1	13	637	188	2	13	618	260	3	11	553	303
1	14	670	201	2	14	649	271	3	12	579	307
				2	15	677	290	3	13	605	318
								3	14	632	332
								3	15	657	351
4	1	325	432	5	2	364	494	6	3	390	545
4	2	348	420	5	3	380	469	6	4	403	522
4	3	369	403	5	4	396	451	6	5	420	503
4	4	389	388	5	5	416	436	6	6	437	490
4	5	411	374	5	6	436	425	6	7	455	479
4	6	434	363	5	7	456	417	6	8	475	470
4	7	457	358	5	8	477	410	6	9	495	468
4	8	479	352	5	9	499	407	6	10	516	467
4	9	502	351	5	10	519	408	6	11	536	475
4	10	525	351	5	11	541	413	6	12	556	485
4	11	547	355	5	12	563	423	6	13	578	506
4	12	570	363	5	13	583	436				
4	13	594	375	5	14	603	453				
4	14	617	390	5	15	620	470				
4	15	642	410								
4	16	667	432								
7	5	427	580								
7	6	440	565								
7	7	455	548								
7	8	474	539								
7	9	491	530								
7	10	511	531								
7	11	531	529								
7	12	552	533								

5.7 Results

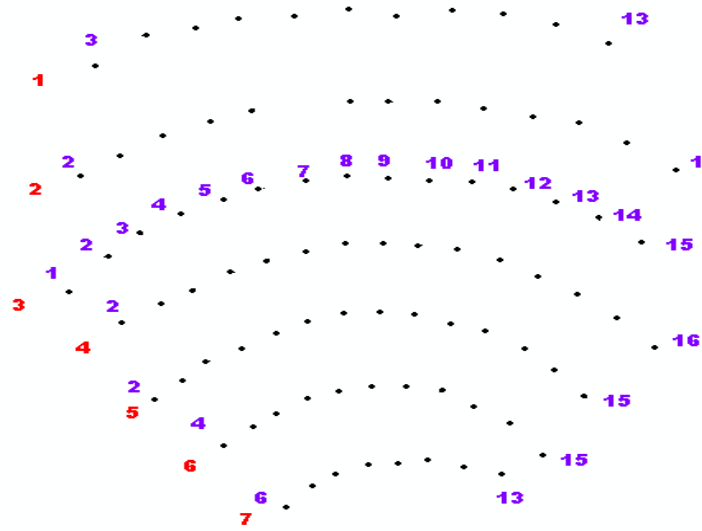
The results obtained for 13 other reflected images are shown below.

1. Test Image 1



(a)

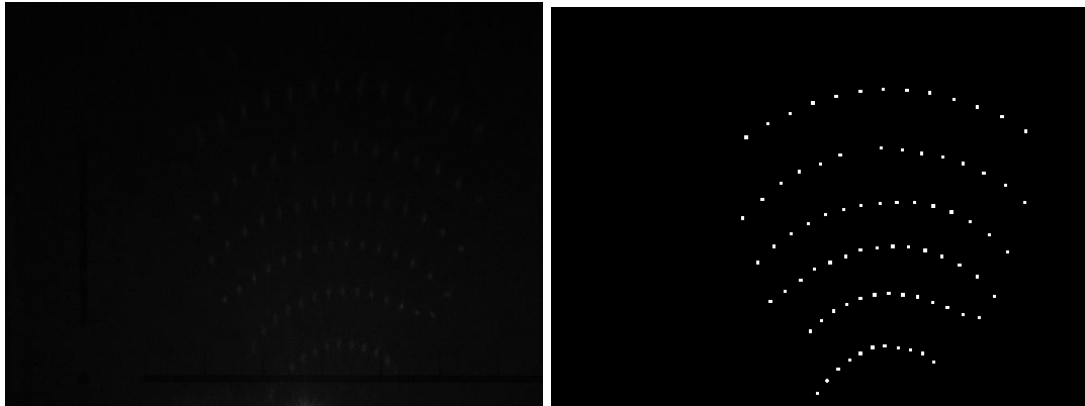
(b)



(c)

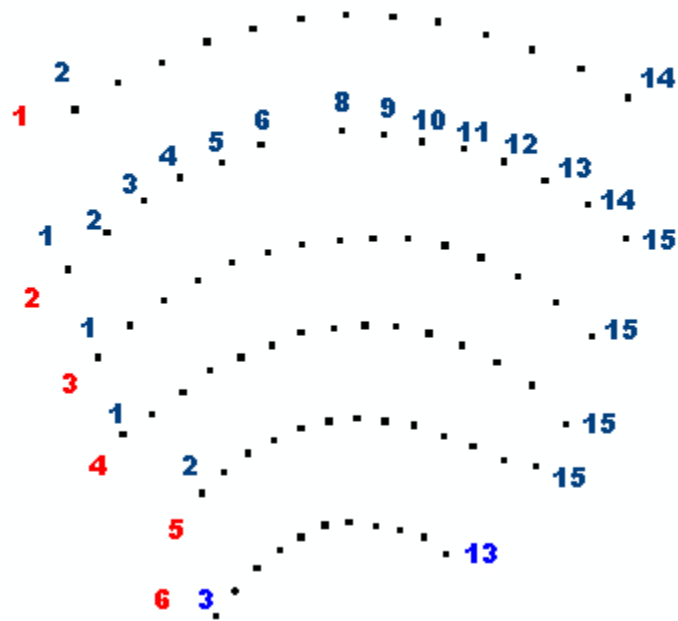
Figure 5-14 (a) Original Image (b) Binary image after segmentation (c) Result of position analysis (the resulting matrix of row and column numbers is depicted on the image)

2. Test Image 2



(a)

(b)



(c)

Figure 5-15 (a) Original Image (b) Binary image after segmentation

(c) Result of position analysis

3. Test Image 3

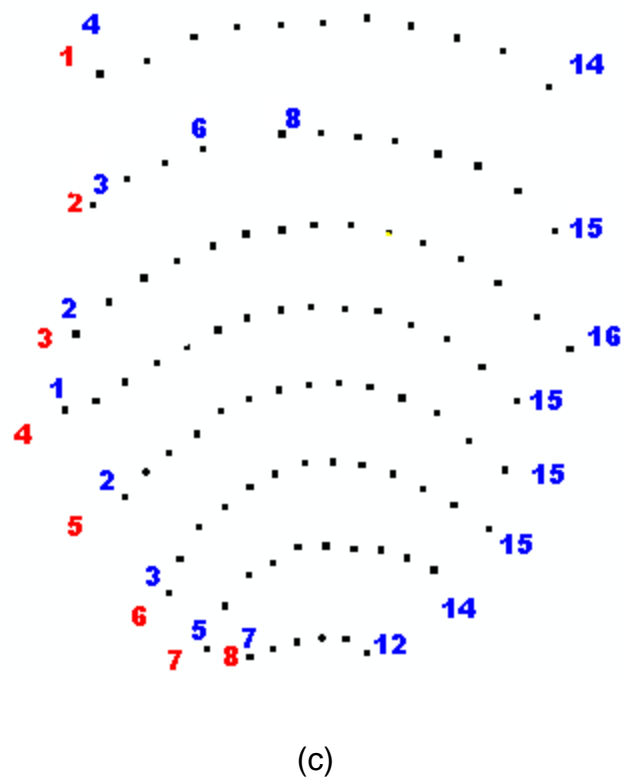


Figure 5-16 (a) Original Image (b) Binary image after segmentation

(c) Result of position analysis

4. Test Image 4

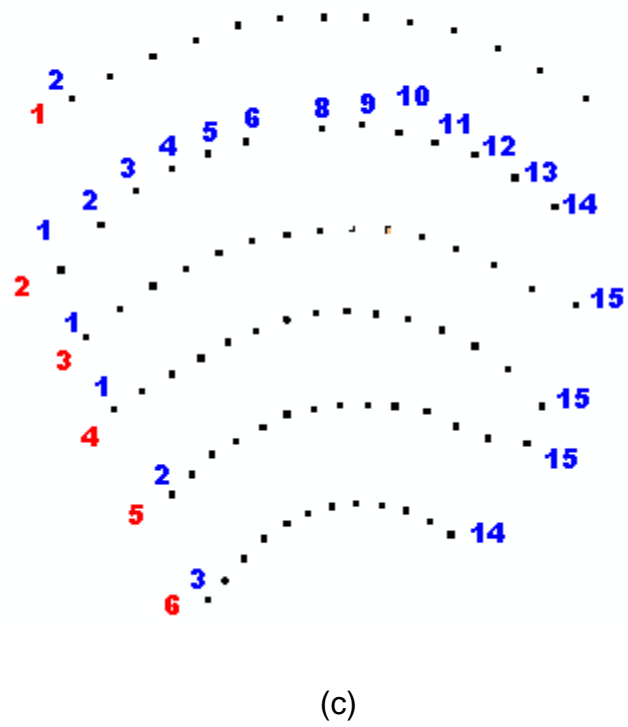
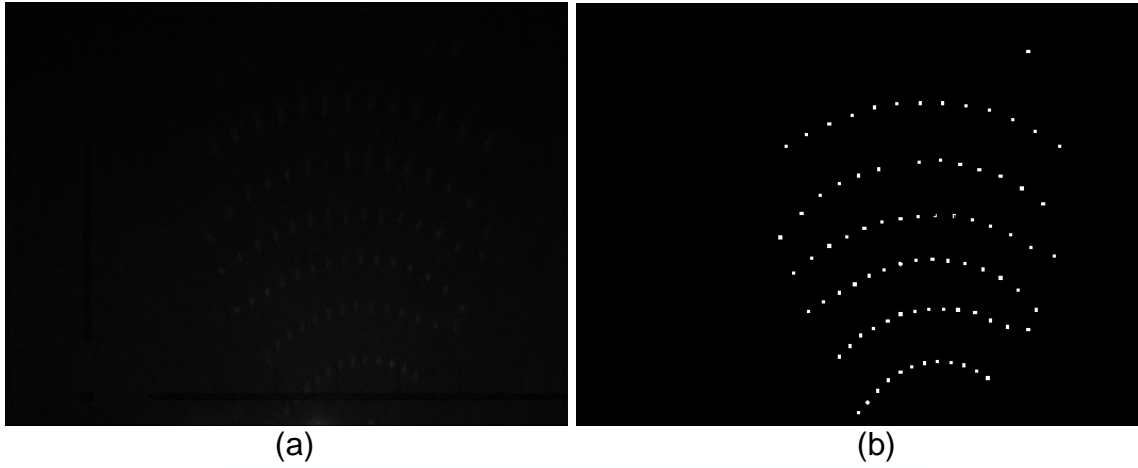
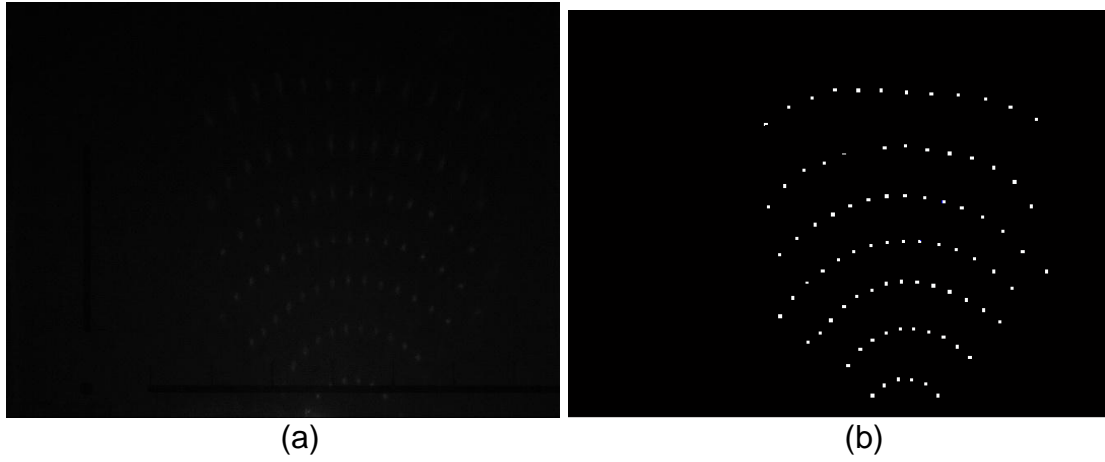


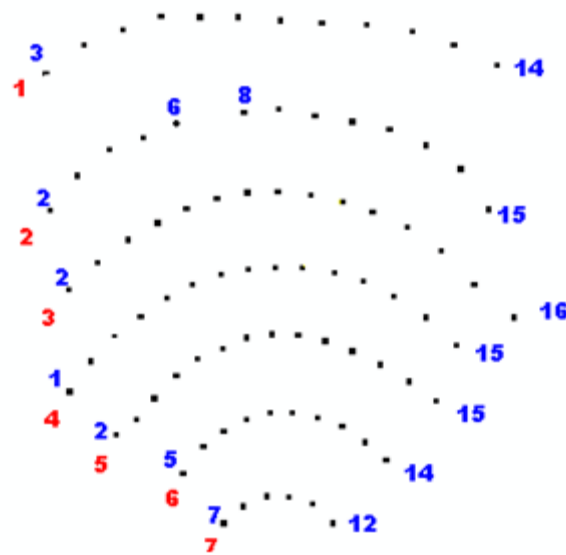
Figure 5-17 (a) Original Image (b) Binary image after segmentation
(c) Result of position analysis

5. Test Image 5



(a)

(b)

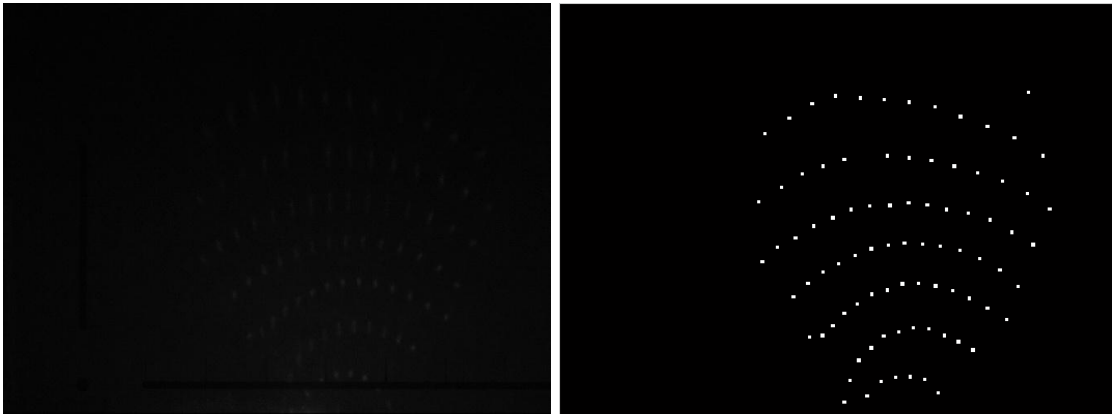


(c)

Figure 5-18 (a) Original Image (b) Binary image after segmentation

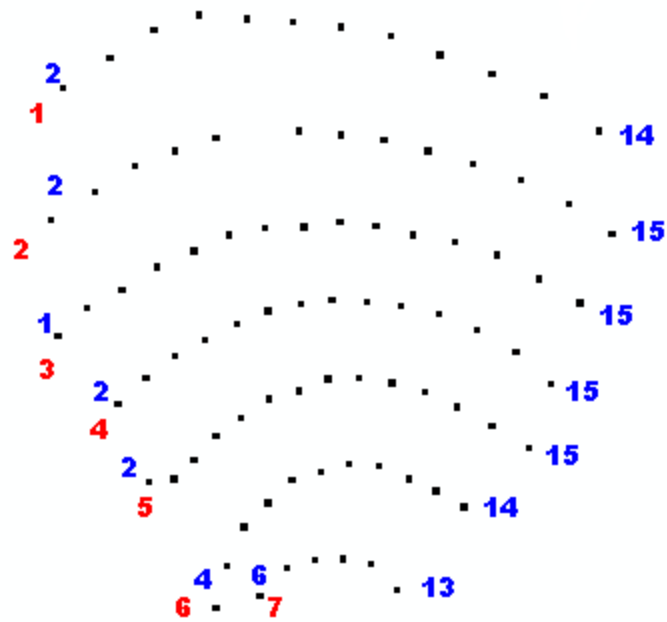
(c) Result of position analysis

6. Test Image 6



(a)

(b)

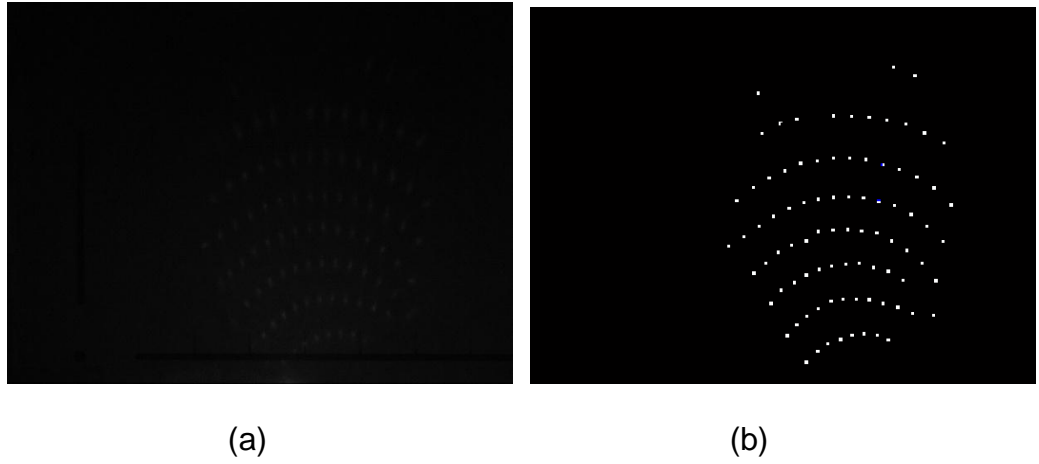


(c)

Figure 5-19 (a) Original Image (b) Binary image after segmentation

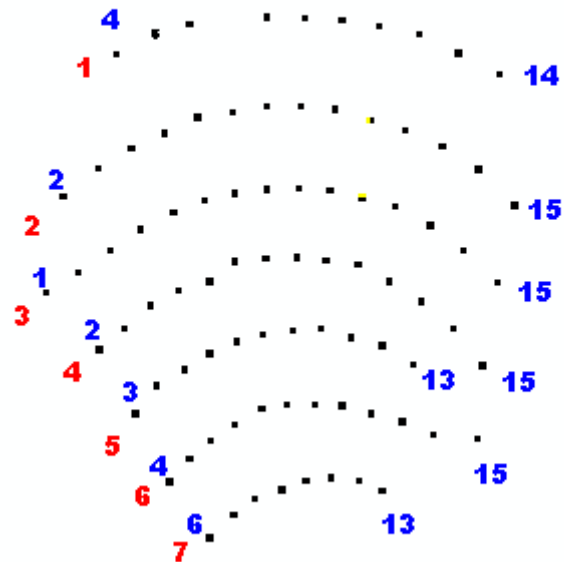
(c) Result of position analysis

7. Test image 7



(a)

(b)



(c)

Figure 5-20 (a) Original Image (b) Binary image after segmentation

(c) Result of position analysis

8. Test Image 8

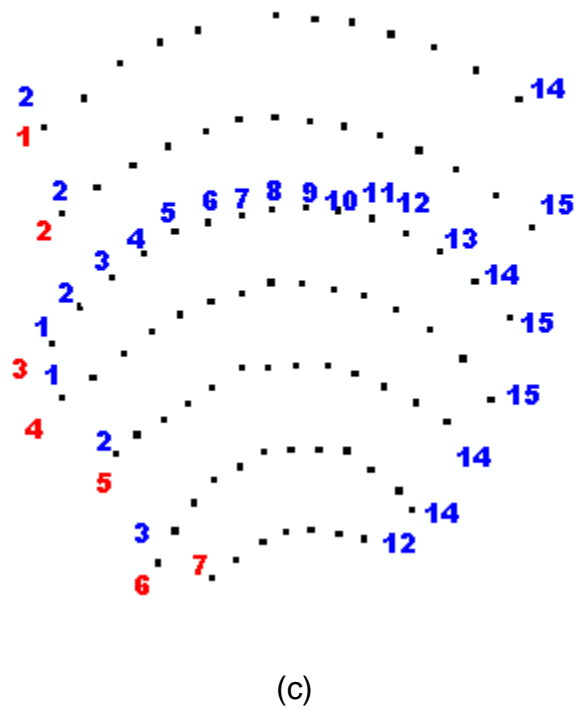
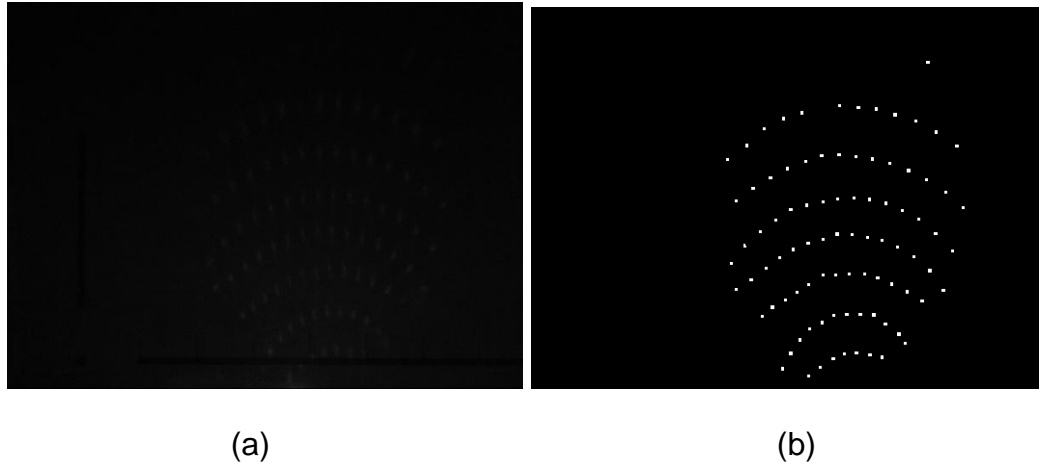


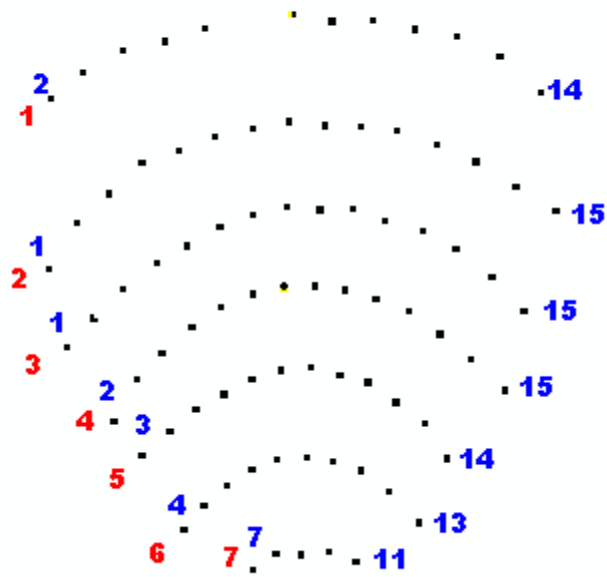
Figure 5-21 (a) Original Image (b) Binary image after segmentation (c) Result of position analysis

9. Test Image 9



(a)

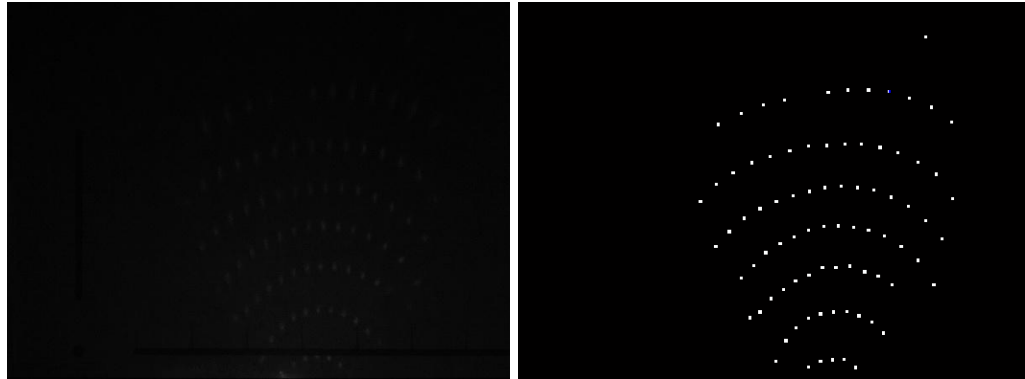
(b)



(c)

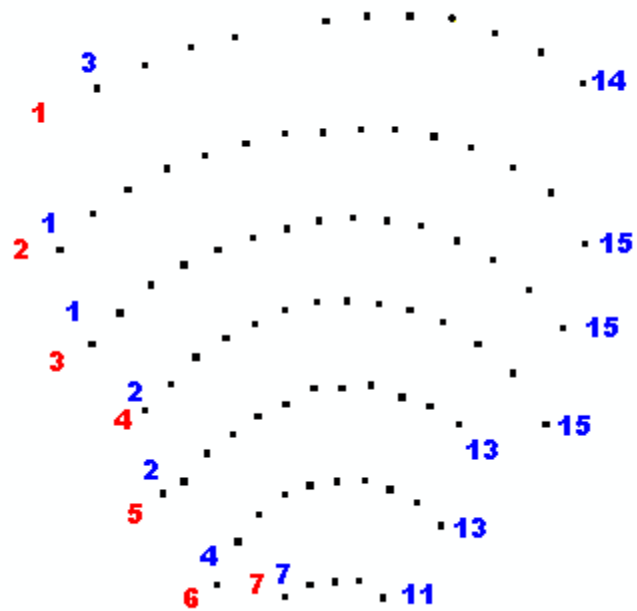
Figure 5-22 (a) Original Image (b) Binary image after segmentation (c) Result of position analysis

10. Test Image 10



(a)

(b)



(c)

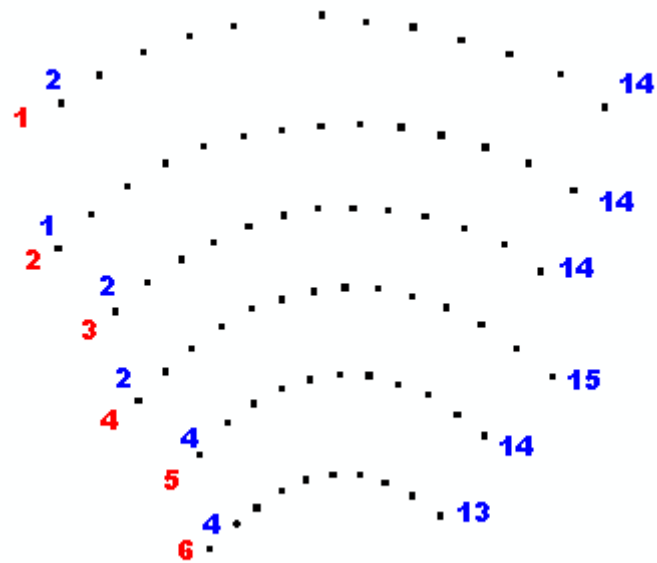
Figure 5-23 (a) Original Image (b) Binary image after segmentation (c) Result of position analysis

11. Test Image 11



(a)

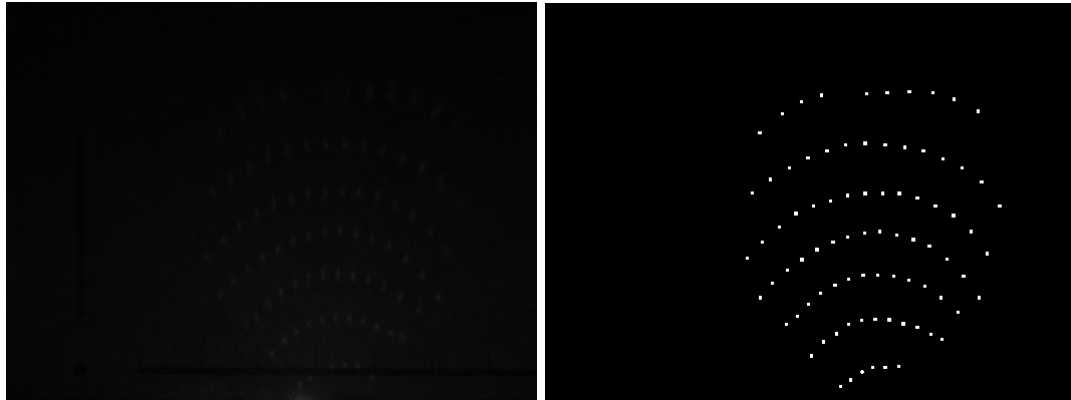
(b)



(c)

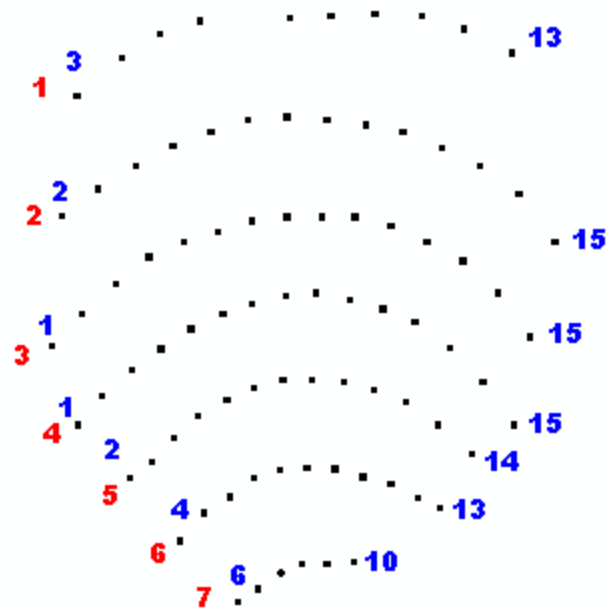
Figure 5-24 (a) Original Image (b) Binary image after segmentation (c) Result of position analysis

12. Test Image 12



(a)

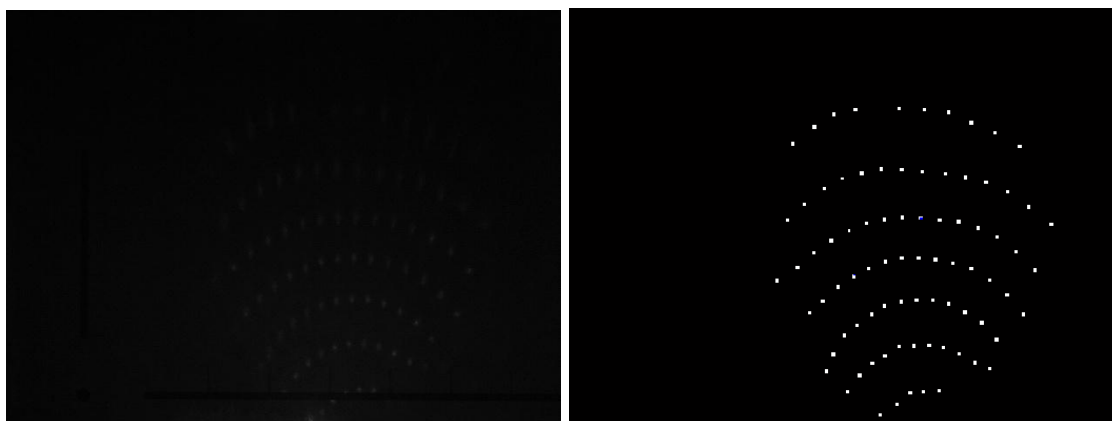
(b)



(c)

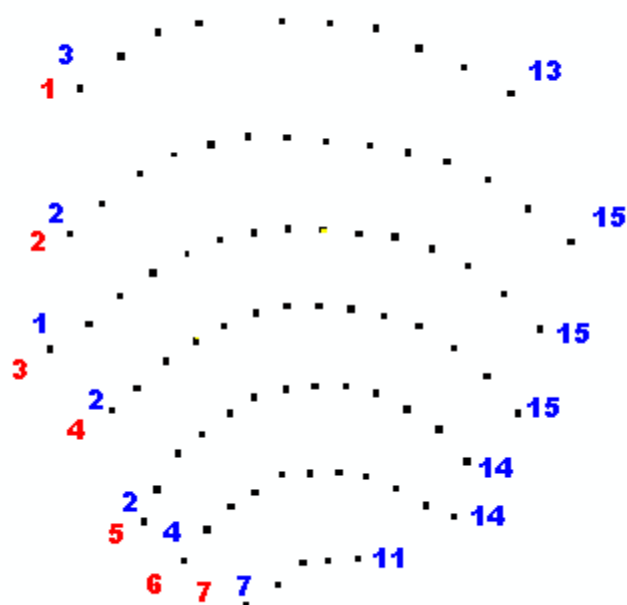
Figure 5-25 (a) Original Image (b) Binary image after segmentation (c) Result of position analysis

13. Test Image 13



(a)

(b)



(c)

Figure 5-26 (a) Original Image (b) Binary image after segmentation (c) Result of position analysis

CHAPTER 6

CONCLUSION AND FUTURE WORK

Welding is a labor intensive process that requires great skill. Automation of this process will result in reduction of costs, consistent quality welds, improved capacity, higher productivity and repeatability. Though the existing welding robots help improve weld productivity, they lack the intelligent capabilities that human welders possess to achieve good quality of welds through observation of the welding process. Weld pool surface measurement is an important step towards the development of next-generation welding machines that mimic the human welder. As an answer to the need for a robust and cost effective method for surface measurement, a vision based sensing method was developed that is based on processing of reflected images. In this thesis, the accuracy of the existing method has been improved by choosing a different welding direction. The new welding direction resulted in a denser reflected dot matrix pattern complicating the image processing algorithms required to process the images. Hence, suitable algorithms have been proposed and implemented in this thesis. The efficiency of the algorithms also has been tested using 15 sample images. The algorithms give good results for all the images.

The major contributions made by this thesis are listed as follows.

1. Improved the accuracy of the existing technique of weld pool surface measurement by choosing a different welding direction.

2. Developed robust Image processing algorithms to effectively analyze the acquired reflected images to extract the position information of each reflected dot. These results may later be used by a surface reconstruction algorithm to reconstruct the surface.

The proposed system used in this dissertation is intended for laboratory experiments and realized only for off-line processing. The future work of this thesis may be realizing a real-time measurement and control since one of the important reasons for establishing the machine vision measurement system is to realize on-line quality control during the welding processes. To achieve this goal, the current image processing algorithms should be simplified and expedited to be suitable for real-time environment.

Also, in order to improve the contrast of the reflected images and ease the image processing algorithm, power of the laser diode must be increased.

Since the density of the projected dot matrix pattern is directly related to system performance, a denser commercial available laser pattern may be applied to improve the sensing system.

REFERENCES

- [1] Groenwald, R. A., Mathieson, T. A., Kedzior, C. T. and Gaid, I.N.C., "Acoustic emission weld monitor system – data acquisition and investigation", *US Army Tank-Automotive Research and Development Command Report ADA085-518*, October 1979.

- [2] Siores, E., "Development of a realtime ultrasonic sensing system for automated and robotic welding", *PhD Thesis*, Brunel University, December 1988.

- [3] Guu A. C. and Rokhlin S., "Computerized radiographic weld penetration control with feedback on weld pool depression", *Mater. Eval.* 47 1204–10, 1989.

- [4] Gohar M. Saeed, "3 Dimensional Measurement of Specular Surfaces and Its Application in Welding Process", *PhD Thesis*, University of Kentucky, 2005

- [5] <http://en.wikipedia.org/wiki/Welding>

- [6] Hongsheng Song, "Machine Vision Recognition of three dimensional specular weld pool surface for Gas Tungsten Arc Weld Pool", *PhD Thesis*, University of Kentucky, 2007

- [7] R. Kovacevic, Y. M. Zhang, and S. Ruan, "Sensing and control of weld pool geometry for automated GTA welding," *ASME Journal of Engineering for*

Industry, 117(2): 210-222, 1995.

[8] R. Kovacevic, Y. M. Zhang, "Real-time image processing for monitoring of free weld pool surface," *ASME Journal of Manufacturing Science and Engineering*, 119(2): 161-169, 1997.

[9] Mnich, C., Al-Bayat, F., Debrunner, C., Steele, J., Vincent, T., "In Situ Weld Pool Measurement using Stereovision", *ASME, Proceedings 2004, Japan – USA Symposium on Flexible Automation*, Denver, Colorado, July 19-21, 2004.

[10] http://en.wikipedia.org/wiki/Gas_tungsten_arc_welding

[11] W. Swaim. "Gas tungsten arc welding made easy," *Welding Journal*, 77(9): 51-52, 1998

[12] R. Kovacevic, Y. M. Zhang, and S. Ruan, "Sensing and control of weld pool geometry for automated GTA welding," *ASME Journal of Engineering for Industry*, 117(2): 210-222, 1995

[13] Mingji Lou, "Computation of Weld Pool Surface from Specular Reflection and Optical Flow", *Master Thesis*, University of Kentucky, 2004

- [14] Guu A. C. and Rokhlin S., "Computerized radiographic weld penetration control with feedback on weld pool depression", *Mater. Eval.* 47 1204–10, 1989.
- [15] Siores, E., "Development of a realtime ultrasonic sensing system for automated and robotic welding", *PhD Thesis*, Brunel University, December 1988.
- [16] Lucas, W. and Maller, R.S., "Automatic control of penetration in pulsed TIG welding", *TWI Members Report P/72/1975*.
- [17] Groenwald, R. A., Mathieson, T. A., Kedzior, C. T. and Gaid, I.N.C., "Acoustic emission weld monitor system – data acquisition and investigation", *US Army Tank-Automotive Research and Development Command Report ADA085-518*, October 1979.
- [18] Chin, B.A., Madsen, N.H. and Goodling, J.S., "Infrared thermography for sensing the arc welding process", *Welding Journal*, Vol. 62 No. 9, September 1983, pp. 227s-34s.
- [19] Madigan, R.B., Renwich, R.J., Farson, D.F. and Richardson, R.W. "Computer-based control of full penetration GTA welds using weld pool oscillation sensing", *First International Conference on Computer Technology in Welding*, Cambridge, 1987, pp. 165-74.

- [20] Richardson, R.W. et al. (1984), "Coaxial arc weld pool viewing for process monitoring and control", *Welding Journal*, Vol.63, No.3, ppl43-50.
- [21] Wu, C. S., Gao, J. Q., Liu, X. F, Zhao, Y. H., "Vision-based measurement of weld pool geometry in constant-current gas tungsten arc welding". *Proc. Instn Mech. Engrs Vol. 217 Journal engineering manufacture*. IMechE 2003.
- [22] Gohar Saeed, "Vision-based sensing of the welding process: a survey", *Int. J. Modeling, Identification and Control*, 2005
- [23] Yu J-Y and Na S J, "Study on vision sensors for seam tracking of height-varying weldment", *Mechatronics* 8, 21–36, 1998
- [24] Bonser G and Parker G A, "Robotic gas metal arc welding of small diameter saddle type joints using multistriple structured light", *Opt. Eng.* 38 1943–9, 1999
- [25] Zhang Y M and Li L, "Interval model based robust control of weld joint penetration", *ASME J. Manuf. Sci. Eng.* 121 425–33, 1999
- [26] Klein M V and Furtak T E, *Optics (New York: Wiley) chapter 3*, 1986

- [27] Saeed G., Lou M. J., and Zhang, Y. M., "Computation of 3D weld pool surface from the slope field and point tracking of laser beams". *Measurement Science and Technology*, 15(2): 389-403, (2004)
- [28] Gonzales R.C., Woods R.E. Digital Image Processing (2nd Edition. PH, 2001)
- [29] Raghuram Rangarajan, Ramji Venkataramanan, Siddharth Shah, "Image Denoising Using Wavelets", December 16, 2002.
- [30] J. Canny, "A computational approach to edge detection", *IEEE Transactions on Pattern Analysis and Machine Intelligence* 8 (6) (1986) 679–698
- [31] <http://www.pages.drexel.edu/~weg22/edge.html>
- [32] http://www.ams.sunysb.edu/~lindquis/3dma/man_3dma/manual/node19.html

VITA

Date of Birth: 29th of July, 1984

Place of Birth: Hyderabad, India

Education:

- Jawaharlal Nehru Technological University, India June 2005

Bachelor of Technology in Electronics and Telematics

Aparna Janga

12/10/07